Tailored Coatings for Enhanced Performance of Zinc-Magnesium Alloys in Absorbable Implants

David Hernández-Escobar[1,2,*], Natalia Pajares-Chamorro[1,*], Xanthippi Chatzistavrou[1,3], Kurt D. Hankenson[4], Neal D. Hammer[5], and Carl J. Boehlert[1]

1. Department of Chemical Engineering and Materials Science, Michigan State University, East Lansing, 48824, Michigan, U.S.A.
2. Now at: Laboratory of Mechanical Metallurgy, École Polytechnique Fédérale de Lausanne (EPFL), Lausanne, 1015, Switzerland
3. Department of Chemical Engineering, Aristotle University of Thessaloniki, Thessaloniki, 54124, Greece
4. Department of Orthopedic Surgery, University of Michigan, Ann Arbor, 48104, Michigan, U.S.A.
5. Department of Microbiology and Molecular Genetics, Michigan State University, East Lansing, 48824, Michigan, U.S.A.

* These authors contributed equally

Abstract

Absorbable metals exhibit potential for next-generation temporary medical implants, dissolving safely in the body during tissue healing and regeneration. Their commercial incorporation could substantially diminish the need for additional surgeries and complications tied to permanent devices. Despite extensive research on magnesium (Mg) and iron (Fe) achieving the optimal combination of mechanical properties, biocompatibility, and controlled degradation rate for absorbable implants remains a challenge. Zinc (Zn) and Zn-based alloys emerged as an attractive alternative for absorbable implants due to their favorable combination of *in vivo* biocompatibility and degradation behavior. Moreover, the development of suitable coatings can enhance their biological characteristics and tailor their degradation process. In this work, four different biodegradable coatings (based on zinc phosphate (ZnP), collagen (Col), and Ag-doped bioactive glass nanoparticles (AgBGN)) were synthesized by chemical conversion, spin-coating, or a combination of both, on Zn-3Mg substrates. This study assessed the impact of the coatings on *in vitro* degradation behavior, cytocompatibility, and antibacterial activity. The ZnP-coated samples demonstrated controlled weight loss and a decreased corrosion rate over time, maintaining a physiological pH. Extracts from the uncoated, ZnP-coated, and Col-AgBGN-coated samples showed higher cell viability, with increasing concentration. Bacterial viability was significantly impaired in all coated samples, particularly in the Col-AgBGN coating. This study showcases the potential of strategic material-coating combination to effectively tackle multiple challenges encountered in current medical implant technologies by modifying the properties of absorbable metals to tailor patient treatments.

Keywords: absorbable metals; biodegradable coatings, cytocompatibility, antibacterial properties

1 INTRODUCTION

Over the last two decades, the field of biomedical implants has attracted considerable attention due to its potential to improve human life (both quality and longevity) by replacing damaged tissue and organs[1]. Metallic implants, renowned for their strength and fracture toughness, have gained popularity in orthopedic, vascular, and tissue engineering applications. However, the long-term presence of permanent metallic implants can lead to complications such as metal ion release and stress shielding, necessitating additional surgeries and causing discomfort, financial burden, and increased infection risk [2–4].

Absorbable metals present a promising avenue for the development of temporary implant devices, addressing the limitations related to the use of corrosion-resistant metals in permanent implant applications. These implants maintain their mechanical integrity during tissue healing and gradually corrode over time, enabling load transfer to the healed tissue[5,6]. Zinc (Zn) has emerged as a compelling alternative for absorbable implants due to its moderate corrosion rate in simulated body fluid [7]. In addition, Zn plays a vital role in numerous body functions, and when released from the implant, its ions seamlessly integrate into normal metabolic activity without causing toxicity[2,8]. Inadequate levels of Zn have been linked to growth impairments, increased susceptibility to infections, and cognitive decline [9,10].

Extensive research on Zn and Zn-based alloys for bone and vascular implants has demonstrated promising cytocompatibility and antibacterial properties. *In vitro* studies on Zn-3Mg alloy have revealed adjustable cytotoxic effects and dose-dependent influences on cell spreading and migration [11–15]. For example, Zn^{2+} concentrations below 80 μM promoted cell viability, proliferation, adhesion, and migration, while above triggered the opposite biological response [14]. Moreover, Zn exposure exhibits antibacterial potential against implant-related pathogens, such as *E. coli*, *P. aeruginosa*, and *S. aureus*, attributed to the release of Zn^{2+} ions from the implant [16,17]. On this basis, controlling the release of Zn^{2+} ions is crucial to minimize the risk of Zn toxicity and enhance the performance of Zn-based implants, which requires further research to understand degradation mechanisms and microenvironment effects [12].

One approach to control the release of Zn^{2+} ions is the design of coatings that can tune the degradation rate. To this end, this study investigates the influence of four different coatings on Zn-3Mg substrates. Each coating was selected based on its potential to enhance cytocompatibility and improve antibacterial properties. For instance, the design of zinc phosphate (ZnP) coatings was inspired by previous investigation on calcium phosphate (CaP) coatings for orthopedic applications. CaP coatings have been successfully synthesized on Zn-based substrates, exhibiting a composition consisting of carbonated apatite like that of natural bone tissue, leading to enhanced bone forming ability and tunable degradation rates [18,19]. While CaP coatings exhibit enhanced bone-forming ability and tunable degradation rates [18], they may not be suitable for implants near highly vascularized regions due to the potential risk on vascular calcification [19]. In this work, replacing Ca for Zn is proposed by synthesizing a ZnP coating, which can simultaneously prevent calcification, enhance compatibility and minimize substrate degradation [18–22].

Collagen Type I coatings, on the other hand, play a fundamental role in the interaction between implants and host tissue. Previous studies in titanium (Ti) and magnesium (Mg) substrates have demonstrated improved cell attachment with collagen-based coatings, however achieving uniformity and preserving the collagen protein structure pose challenges [22,23]. In this work, we develop a Collagen Type I coating on Zn-3Mg substrates to enhance cell attachment using a simplified synthesis protocol that dispense with the use aggressive chemicals, ensuring preservation of protein structure and homogeneity.

Bioactive glass coatings have been widely applied in biomedical implants to enhance biocompatibility and bioactivity with the host tissue. The versatility of bioactive glasses enables the incorporation of additional dopants, such as silver (Ag), to enhance antibacterial activity [24–30]. In this work, we propose an Ag-doped bioactive glass nanoparticle (AgBGN) based coating, in a Collagen Type I matrix, which exhibited potential to simultaneously enhance biocompatibility and antibacterial properties of the substrate.

The aim was to tailor the corrosion properties, cell viability, and antibacterial activity. The overarching goal was to reduce the Zn^{2+} release rate, enhance the *in vitro* biocompatibility, and improve the antibacterial properties. Because Zn-3Mg is a relatively new material being investigated, we are unaware of any literature identifying antibacterial and corrosion properties for this alloy and therefore it is unclear if such related problems exist. Finally, the *in vitro* degradation, cytocompatibility, and antibacterial behavior of the different coated substrates was assessed and compared to that of the uncoated control samples.

2 EXPERIMENTAL METHODS

2.1 Synthesis of coatings

As-cast Zn-3Mg alloy bars, purchased from Goodfellow Corportation (Pittsburgh, Pennsylvania, USA), were subjected to an homogenization heat treatment (360 ± 2 ºC for 15 h inside a vacuum sealed (~ 10^{-4} torr) quartz tube followed by water quenching[31]) and cut into disks of ~ 10 mm diameter and 1 mm thickness. This heat treatment successfully homogenized the microstructure with respect to the phase compositions and distributions [31]. The disks were ground using SiC abrasive papers up to 1200 US grit size to obtain the experimental samples, referred to as "Zn-3Mg substrates" hereafter, which were coated as detailed below.

The coatings were synthesized using the following reagents: zinc nitrate hexahydrate ($Zn(NO_3)_2{\cdot}6H_2O$), phosphoric acid (H_3PO_4), and sodium hydroxide (NaOH); all purchased from Sigma Aldrich (St. Louis, MO). Collagen Type I solution (3 mg/mL) PureCol was purchased from Advanced BioMatrix (Carlsbad, CA) and stored at 2-10 ºC to prevent degradation. Phosphate buffered saline (PBS) 10X was purchased from ThermoFisher Scientific (Waltham, MA).

2.1.1 Zinc phosphate coating

The zinc phosphate coatings were synthesized on the Zn-3Mg substrates through a chemical conversion method at room temperature (RT), inspired by the work of Su *et al.* [22] in pure Zn. First, a 0.5 M H_3PO_4 solution was prepared by dissolving 7.35 g H_3PO_4 in 150 mL deionized (DI) water. Second, a 1 M NaOH solution was prepared by dissolving 1.6 g in 40 mL DI water. Third, a 0.14 M $Zn(NO_3)_2$ solution was prepared by adding 1.041 g of $Zn(NO_3)_2{\cdot}6H_2O$ in 24.622 mL DI water under magnetic stirring. Note that the zinc nitrate is hydrated, which adds 0.378 mL extra water to the solution, such that the 0.14 M $Zn(NO_3)_2$ solution volume was 25 mL. Fourth, 15 mL of the 0.5 M H_3PO_4 solution were added to the 0.14 M $Zn(NO_3)_2$ solution. The pH was adjusted from 1.37-1.47 to 2.5 by the dropwise adding approximately 5 mL of the 1 M NaOH solution, bringing the solution volume to 45 mL. Finally, the total volume of the solution was adjusted to 50 mL with DI water. This zinc phosphate solution, as well as the coatings resulting from it, are referred to as ZnP hereafter.

Right before the coating procedure, the Zn-3Mg substrate was slightly polished with 1200 US grit size SiC paper for 20-30 s to ensure a fresh non-oxidized surface layer. The sample was first ultrasonically cleaned for 20-30 s in ethanol, rinsed thoroughly with ethanol and dried with a compressed air stream for 10-20 s. Then, the sample was immersed for 5 min in a beaker containing 50 mL of the prepared ZnP solution

following the synthesis protocol described by Su *et al.* [22]. Finally, the sample was removed from the ZnP solution, rinsed thoroughly with DI water and dried in air. It is noted that the coating morphology was more uniform when these steps were conducted one right after the other (i.e., minimizing time between different steps). Therefore, the ZnP coatings were performed one at a time.

2.1.2 Collagen coating

A Collagen Type I coating solution was applied onto Zn-3Mg substrates using the spin-coating technique for the first time. This technique enables both the production of uniform thin films and the potential to scale up [32]. The preparation of the collagen solution was performed in sterile conditions inside a laminar flow biosafety cabinet, all the materials involved were sterilized under ultraviolet (UV) light inside the biosafety cabinet. The NaOH (0.1 M) solution and the distilled water had been previously sterilized by filtering through a 0.22 mm syringe filter, and thus, were not UV sterilized. Similarly, the PBS (10X) and PureCol solution (3 mg/mL) were maintained in sterile conditions.

The PureCol solution was used to prepare a 3-D gel according to manufacturer recommendation to obtain 2 mL of solution. During this process, all reagents were maintained in ice to prevent the premature polymerization of the collagen. First, 1 part (0.2 mL) of chilled 10X PBS was added to 8 parts (1.6 mL) of PureCol with gentle swirling using the vortex mixer. Second, the pH of the mixture was adjusted to 7.0-7.5, monitoring the pH with paper strips, by adding 0.10-0.15 mL of 0.1 M NaOH solution. Third, the final volume of the solution was adjusted with distilled water (0.05-0.1 mL) to a total of 10 parts. The resulting collagen solution had a concentration of 2.4 mg/mL and was maintained at 2-10 ºC to prevent gelation before spin-coating. This collagen solution, as well as the coatings resulting from it, are referred to as Col hereafter. This collagen solution was also diluted to 1 mg/mL to investigate an alternative collagen concentration.

For spin-coating, the Zn-3Mg substrate sample was secured in the spin-coater (Chemat Technology Spin Coater KW-4A) under vacuum. All the spin-coatings were performed at 3000 rpm for 20-30 s by pipetting 150 μL of the chilled Col solution on the center of the substrate surface. The spin-coated substrate was transferred to an incubator, at 37 ºC, for 90-120 min for gelation. Spin-coated substrates were coded using a ColX_Y nomenclature, where X was the concentration of collagen in mg/mL (i.e., 1 or 2.4) and Y was the spin-coating time in s (i.e., 20 or 30).

In addition, a dual coating consisting of ZnP and Col was developed with the goal of modifying the degradation behavior of Zn-3Mg substrate and improving its biocompatibility simultaneously. First, the ZnP coating was developed by chemical conversion, and then, the ZnP coated substrates were spin-coated with a Col solution of 2.4 mg/ml using 3000 rpm for 20 s. These samples are referred to as “ZnP-Col” hereinafter.

2.1.3 Collagen-based bioactive glass nanoparticle coating

The AgBGN used to develop the coatings were previously synthesized by a modified Stöber method with a composition of SiO_2 59.6 – CaO 25.5 – P_2O_5 5.1 – Al_2O_3 7.2 – Ag_2O 2.2 (wt. %) [26,33]. These AgBGN were surface functionalized with polyethylene glycol (PEG) to facilitate nanoparticle dispersion for enhanced coating uniformity. The resulting Col-based AgBGN coating will be referred to as “Col-AgBGN” hereafter and was prepared as follows. First, 20 mg of AgBGN were dispersed in 20 mL of distilled water under agitation at 500 rpm. Second, 400 mL of a 10 mM PEG solution in H_2O were added into the 1 mg/mL AgBGN solution and mixed at 500 rpm for about 30 min. Third, the AgBGN-PEG mixture was centrifuged, the supernatant was discarded, and 4 mL of distilled water were added to obtain a 5 mg/mL solution of

AgBGN-PEG. Fourth, 1 mL of the 5 mg/mL AgBGN-PEG solution was centrifuged for 2 min at 1000 rpm, and the supernatant was replaced by 1 mL of 2.4 mg/mL Col solution. Finally, 130 μL of the resulting Col-AgBGN solution were added onto the center of the Zn-3Mg substrate and spin-coated for 20 s at 3000 rpm.

2.2 Microstructural characterization of the coated samples

2.2.1 Scanning electron microscopy

A JEOL JSM-7500F SEM coupled with EDS was used to examine the morphology and to estimate the chemical composition of the coatings, which was further investigated by grazing incidence XRD. EDS elemental maps were acquired at an accelerating voltage of 10 kV and working distance of 8 mm for the ZnP-coated samples to investigate the elemental distribution. A Zeiss Auriga FIB-SEM was used to mill a portion of the coatings to estimate their thicknesses.

To preserve the structure of the Col-containing samples (i.e., Col, ZnP-Col and Col-AgBGN) during SEM imaging, they were previously dehydrated and dried as specified below. The dehydration procedure consisted of immersing the Col-containing samples in a series of ethanol/distilled water dilutions of 25%, 50%, 75% and 100% (three times) (vol. %) for 10 min each. Samples were directly transferred from one dilution to the next every 10 min, preventing them from drying in between dehydration steps. Immediately after dehydration, the samples were dried by hexamethyldisilazane (HMDS) evaporation through a series of immersion steps in ethanol/HMDS dilutions of 33%, 50%, 66% and 100% (two times) (vol. %) for 15 min each. Like in the dehydration process, samples were transferred from one dilution to the next one every 15 min. When the samples were immersed in the last step of 100% HMDS, the 24-well plate was left capped loosely in the fume hood overnight for HMDS evaporation. After drying, the samples were sputter coated with a Pt target for 30 s at 30 mA by using a Denton Desk II sputter coater to prevent surface charging during SEM imaging.

2.2.2 Grazing incidence X-ray diffraction

Grazing incidence X-ray diffraction (GIXRD) enables the characterization of thin films and coatings by using small incident angles for the incoming X-ray beam, such that the penetration depth of X-rays is very limited, and thus, diffraction information is highly surface sensitive. Unlike in the Bragg-Brentano configuration, in the GIXRD scan the incident grazing angle is fixed while the detector rotates over a 2θ range. In GIXRD, the critical angle of a material is defined as the incident angle below which the X-ray is fully reflected from the material surface. Therefore, a GIXRD measurement with a grazing incidence angle close to the critical angle would be inherently probing the material surface. Under this condition, the incident X ray is nearly parallel to the material surface, and typical grazing incidence angles are between 0.2-2 º [34].

GIXRD was performed in the uncoated and ZnP coated samples (before and after the immersion testing). The critical angle (Θ_c) was calculated in degrees using Equation [34], from the X-ray refractive index of the material (d), which was previously obtained using the online tool (https://henke.lbl.gov/optical_constants/getdb2.html)

$$\Theta_c = \sqrt{2\delta} * \frac{180}{\pi}$$ Equation 1

For the stoichiometric composition of ZnP, $Zn_3(PO_4)_2$, a d value of $2.16 \cdot 10^{-5}$ was obtained, which resulted in a Θ_c value of 0.377 º. Thus, a minimum Θ_c value of 0.38 º was chosen for all the GIXRD scans.

2.3 *In vitro* degradation and corrosion resistance of coated samples

The *in vitro* degradation behavior and corrosion resistance were evaluated by immersion of the samples for 21 days in Dulbecco´s Modified Eagle´s Medium (DMEM) from Sigma Aldrich (Saint Louis, MO). Immersion testing was performed inside an incubator at 37 ºC and half of the DMEM immersion volume was refreshed, after measuring the pH, every other day to mimic physiological conditions. The collected immersion medium was stored at 4 ºC. Two conditions of the Zn-3Mg alloy substrates, uncoated and ZnP coated, were studied in triplicates to ensure reproducibility. The decision to exclude testing of the Col-coated samples was based on the assumption that the Col coating would degrade rapidly in a physiological environment and therefore have negligible impact on the corrosion resistance.

The immersion test was conducted following the guidelines outlined in ASTM G31-12a: "Standard Guide for Laboratory Immersion Corrosion Testing of Metals" [35]. The ratio between the immersion volume and the exposed surface area was set at 20 mL/cm^2. Each sample, with a total exposed surface area of approximately 1 cm^2. To maintain the test conditions, half of the volume (i.e., 10 mL) of DMEM were refreshed every 2 days. Individual plastic containers with a diameter of 36 mm were used to isolate each sample throughout the test. The containers were kept capped throughout the immersion experiment, except during media replacement, to prevent degradation of the DMEM.

Corrosion rate estimation was conducted at three time points (day 6, 12, and 21) during the immersion period. Surface characteristics were examined using scanning electron microscopy (SEM) and compositional changes were analyzed using energy-dispersive X-ray spectroscopy (EDS) at two time points (day 6 and 21). Prior to the immersion test, grazing incidence X-ray diffraction (GIXRD) measurements were performed, both before and after the 21-day immersion. At each time point (6, 12, and 21 days), triplicate samples for each material condition were carefully removed from the immersion test, thoroughly rinsed with distilled water, and air dried at room temperature. The samples were then weighed using a precision scale. To remove corrosion products, ultrasonic cleaning was performed using a solution of 200 g/L CrO_3 in water, following ASTM G1-03 guidelines. After rinsing with distilled water, the samples were reweighed to estimate the corrosion rate using Equation 2 as specified in ASTM G1-03 [36].

$$CR = K\frac{w_i - w_f}{A\,t\,\rho} \qquad \text{Equation 2}$$

where CR is the corrosion rate in mm/year, K is a time conversion coefficient equal to $8.76 \cdot 10^7$, w_i and w_f are the initial and final weight of the sample in g, A is the sample area exposed to solution in cm^2, t is the immersion time in h, and ρ is the density of the material in g/cm^3.

2.4 Cytocompatibility evaluation of coated samples

In this work, the indirect method was performed to assess the cellular response to the sample extracts, which are degradation products derived from the samples. Various concentrations of these extracts were used to avoid any potential interference between the Zn-3Mg alloy substrate and the cell counting assays. Three different samples were evaluated: uncoated, ZnP, and Col-AgBGN. Note that uncoated samples refer to the Zn-3Mg alloy substrate *per se*. The tests were performed in triplicates for statistical analysis.

2.4.1 Preparation of sample extracts

UV-sterilized samples (i.e., Uncoated, ZnP coated and Col-AgBGN coated) were immersed for 3 days in cell culture medium at a surface area to volume ratio of 1.25 cm^2/mL, following ISO 10993-5 recommendations [37]. The incubation was carried out at 37 ºC and 5% CO_2 for 3 days. The cell culture medium contained 16.5 % fetal bovine serum (FBS), 1 % Antibiotic/Antimycotic, and 1 % L-glutamine in α-minimum essential medium (α-MEM (-)). All the extracts were collected after 3 days of immersion under sterile conditions.

For the indirect *in vitro* cytotoxicity tests, extracts were diluted in fresh cell culture medium based on the reported 6-fold to 10-fold dilution range that mimics the human body environment [38]. Even though this recommendation was originally proposed for Mg-based materials, researchers in Zn-based materials since 2015 have been using the same approach consistently. Thus, three extract dilutions were prepared for each material condition: 10-fold (10% extract concentration), 6-fold (16.7% extract concentration), and 4-fold (25% extract concentration). The diluted extracts were stored at 4 ºC until use.

2.4.2 Preparation of cell culture

Human marrow stromal cells (hMSC) 7043L were purchased from the Center for Gene Therapy, Tulane University. Thawed cells were cultured at a density of 3000-5000 cells/cm² in a humidified incubator (37 ºC, 5% CO_2). Cell expansion was carried out in T75 flasks with medium renewal every 2-3 days. Upon reaching 80% confluency, cells were washed with PBS and detached using trypsin for 2-3 minutes. Trypsin activity was stopped by adding an equal volume of fresh media, and the cells were collected by centrifugation (5 min, 1200 rpm). The supernatant was discarded, and the cell pellet was resuspended in fresh media for cell counting using a hemocytometer. The desired cell densities were then plated in 12-well or 24-well plates. Cells for these *in vitro* studies were used in passage 4 to 6.

2.4.3 Evaluation of cell proliferation

The Cell Counting Kit-8 (CCK-8) colorimetric assay (abcam, ab228554), assay was used to quantify cell viability. CCK-8 solution was added to the wells, and absorbance at 460 nm was measured after incubation. Cells at passage 6 were seeded at a density of $2.5 \cdot 10^3$ cells/cm² in 24-well plates for the indirect contact proliferation assay, see Figure 1. After cell attachment, the medium was replaced with sample extracts. The 4-fold, 6-fold and 10-fold dilutions of each extract type (i.e., Uncoated, ZnP, and Col-AgBGN), prepared as detailed in 2.4.1, were tested in triplicate. Cell proliferation was evaluated through CCK-8 measurements in a separate 96-well plate at three time points: 2, 4, and 6 days. After each time point, cells were cleaned with PBS to eliminate any CCK-8 residues and the culture media was refreshed with their corresponding extract dilutions. Statistical significance was determined using the student's t-test ($p < 0.05$), and cellular health was monitored by optical microscopy (OM).

2.5 Bacterial adhesion and viability assessment on coated samples

The colonization competition between microorganisms and host cells, known as the "race for the surface," occurs following the implantation of foreign materials in the body. The ability of Zn-3Mg alloy substrates to resist bacteria colonization was evaluated *in vitro.* Four types of coated samples were examined: ZnP, Col, ZnP-Col, and Col-AgBGN. Uncoated samples as well as untreated bacteria (i.e bacteria dispersed in medium) served as controls. The tests were performed in triplicates for statistical analysis. Methicillin-resistant *Staphylococcus aureus* (MRSA) was the bacterium selected for this experiment, as it is one of the most prevalent causes of implant-related infections. Laboratory-derived MRSA USA300 JE2[39] was

cultured on tryptic soy agar and grown overnight at 37°C. A concentrated bacterial solution of approximately 10^7 colony forming units (CFU)/mL was prepared in tryptic soybean broth (TSB) by adjusting the optical density (OD) of the bacterial suspension at 600 nm ($OD_{600\ nm}$) to 0.5.

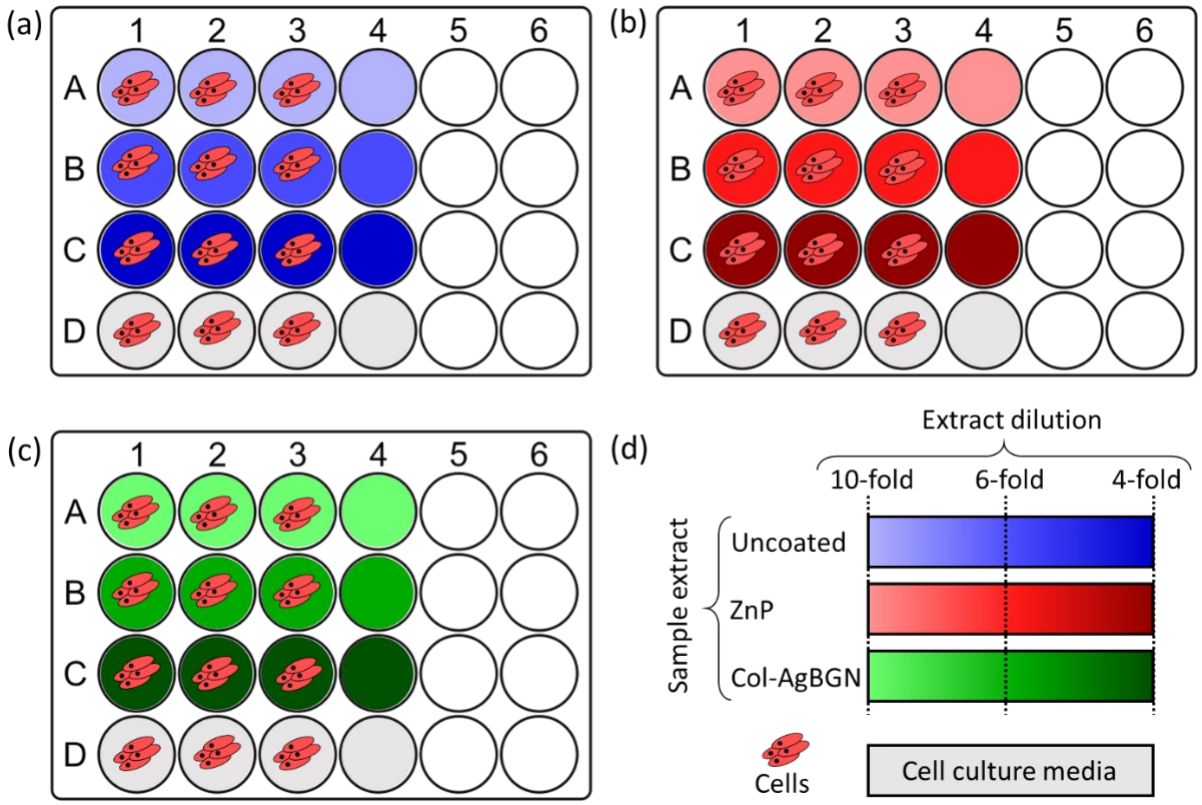

Figure 1: Schematic of the experimental design for the indirect contact *in vitro* proliferation assay with sample extracts from (a) uncoated, (b) ZnP coated and (c) Col-AgBGN coated samples; (d) Key to interpret the different colors and tones in the 24-well plates displayed in (a), (b) and (d).

2.5.1 Assessment of bacteria viability in suspension

The capability of the different samples (i.e. uncoated and coated substrates) to resist MRSA colonization was evaluated by immersing them in 1 mL of the bacteria suspension (OD_{600} = 0.5) in TSB. UV-sterilized samples were placed in triplicate wells of a non-adherent 24-well plate (Nunclon™ Sphera™, ThermoFisher Scientific) to prevent bacteria adhesion to the bottom of the wells. Three empty wells containing 1 mL of the bacterial suspension served as controls (i.e untreated bacteria). The plate was incubated at 37 ºC for 7 days. Bacterial concentration in each of the wells was measured at 1, 2, 3, 5 and 7 days by spectrophotometrically analyzing a 10-fold dilution of the culture at $OD_{600\ nm}$. The bacterial concentration reflects the level of colonization on the sample surface, with higher concentrations indicating reduced attachment.

2.5.2 Bacterial viability and adhesion on coated surfaces

Bacterial colonization was also evaluated by analyzing the adhered bacteria on the sample surface using the live/dead BacLight™ Bacterial Viability kit (L7012, ThermoFisher Scientific). The staining protocol recommended by the manufacturer was followed, where a solution of propidium iodide and SYTO 9 stains

was prepared. SYTO 9 stains fluorescently label bacteria with intact cell membranes, appearing green, while propidium iodide stains bacteria with damaged membranes, appearing red.

After 7 days of incubation in the bacteria suspension, the samples were collected and washed three times for 10 min each with a filtered 0.85 % NaCl solution in distilled water. Then, 0.15 mL of stain solution was added to each sample, covering the surface, and incubated for 25 min at RT in the dark. The stain solution was aspirated, and the samples were washed three times for 10 min with a filtered 0.85 % NaCl solution in distilled water. Manipulation of stained samples was performed in the absence of natural light, as much as possible, to prevent degradation of the stain.

To preserve the morphology of the bacteria while killing them, stained samples were fixed by immersion in a solution containing 2.5 % glutaraldehyde, 2.5 % paraformaldehyde and 0.1 M cacodylate buffer in distilled water for 2 h at RT. After fixation, the samples were washed once with filtered distilled water before air drying [30,40].

Observation of the samples we carried out using a Nikon C2 confocal laser scanning microscope (CLSM) with a Nikon Eclipse NI-U upright configuration. A 40x magnification Plan Fluor dry objective (numerical aperture = 0.75) was used. The excitation/emission maxima for the stains used are 480/500 nm for SYTO 9 and 490/635 nm for propidium iodide. The CLSM images, with a resolution of 1024 pixels x 1024 pixels, were acquired using Kalman averaging for noise reduction and processed with Nikon NIS-Elements software. The live and dead bacteria were quantified based on the number of green and red pixels in the CLSM images, respectively, as described in the Supplemental Information.

2.5.3 Observation of bacteria adhered to coated surfaces

The distribution and morphology of MRSA adhered to the sample surface was observed after 7 days of incubation. Samples were collected from the wells and washed twice for 10 min with filtered distilled water and then immersed in a fixative solution for 2 h. The fixative solution contained 2.5% glutaraldehyde, 2.5% formaldehyde and 0.1 M cacodylate buffer in distilled water to kill bacteria while preserving their morphology [30,40]. After washing with 0.1 M cacodylate buffer for 15 min, samples underwent dehydration by successive immersions in ethanol/distilled water dilutions (25 %, 50 %, 75 % and 100 % (vol.%)) for 5 min each, repeating the last step of immersion in 100% ethanol twice. Dehydrated samples were transferred to the critical point dryer (Leica Microsystem model EM CPD300), where ethanol was replaced by CO_2. Finally, the samples were coated with Os for 15 s to obtain a 10 nm conductive layer before observation in SE mode using a JEOL JSM-7500F SEM operated at an accelerating voltage of 5 kV and a working distance of 4-5 mm. Live and dead bacteria on the sample surface were identified based on their morphology, in comparison with such analysis from the literature. The density of adhered bacteria observed in the SEM was compared with that estimated from the CLSM images.

3 RESULTS

3.1 Surface morphology and characteristics of coatings

3.1.1 ZnP coatings

The surface morphology of the as-homogenized Zn-3Mg alloy samples (uncoated conditions) exhibited a eutectic lamellar microstructure consisting of Zn phases (brighter) and Mg_2Zn_{11} phases (darker) as presented in Figure 2 (a) and Figure 2 (b). The energy dispersive spectroscopy (EDS) analysis of these phases was provided in a previous work [31]. After immersion in the ZnP solution for 5 minutes, a uniform

layer of randomly oriented flake-like crystals, with approximately 2-3 μm diameter pores, formed on the sample surface (Figure 2 (c) and Figure 2 (d)).

The nucleation of platelet crystals was observed at multiple locations on the substrate upon immersion, and these grew over time covering the entire surface of the sample after 5 min. The formation of zinc phosphate hydrate (hopeite), with a chemical composition of $Zn_3(PO_4)_2 \cdot 4H_2O$ was confirmed at the surface of the ZnP sample by GIXRD. Some ZnP coated samples exhibited regions with flower-like structures, resulting from the coalescence of neighboring nucleation sites that grew faster than others (Figure 3 (a)). EDS analysis revealed a uniform elemental distribution of Zn, P and O in the ZnP coating, with higher intensity areas on the EDS Zn map corresponding to the pores in the coating (Figure 3(a) and Figure 3 (b)). The approximate thickness of the ZnP coating was ~ 1 mm (Figure 3 (c)).

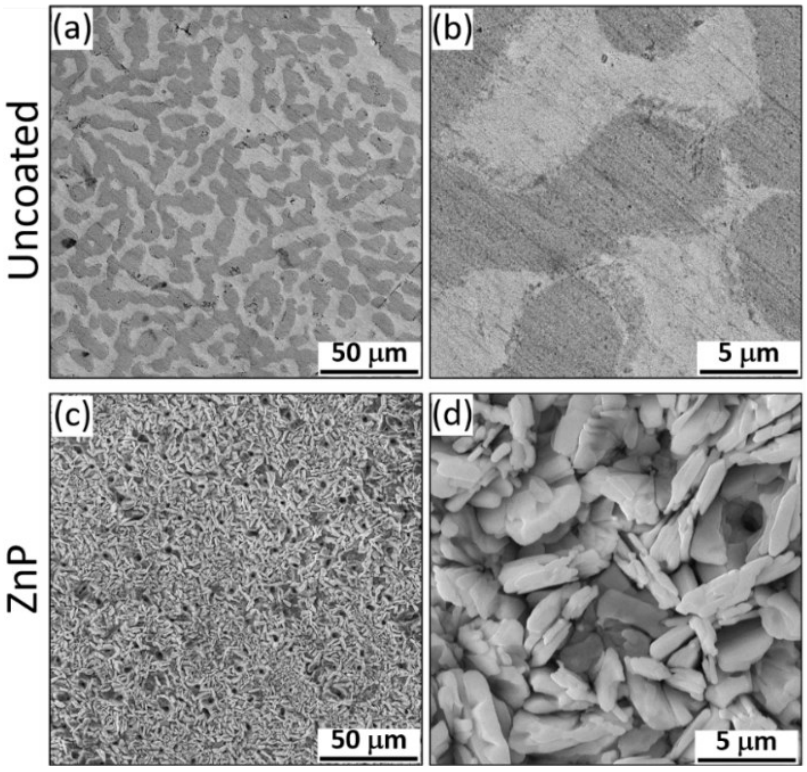

Figure 2: SE-SEM photomicrographs showing the surface morphology of the Zn-3Mg alloy (a-b) uncoated, with a eutectic lamellar microstructure of Zn phases (brighter) and Mg_2Zn_{11} phases (darker), and (c-d) after the zinc phosphate (ZnP) chemical conversion coating, with a flake-like microstructure with uniformly distributed pores.

3.1.2 Col coatings

The surface morphology of the different Col coatings developed by spin-coating at 3000 rpm are presented in Figure 4. The spin-coating of a 2.4 mg/mL PureCol solution for 20 seconds resulted in a uniform distribution of Col fibrils with a thickness of approximately 20-30 nm, randomly oriented on the sample surface (Figure 4 (a)). Increasing the spin-coating time by 10 s, while maintaining the same PureCol concentration, led to a less uniform coating with a lower amount of Col fibrils, which were only observed in specific regions of the sample (Figure 4 (b)). A Col coating produced with a 1.0 mg/mL PureCol solution for 30 seconds exhibited barely distinguishable Col fibrils (Figure 4 (c)). It was noted that the polishing

lines were still evident in the Col coated sample surfaces, suggesting that the Col coatings had submicron thicknesses.

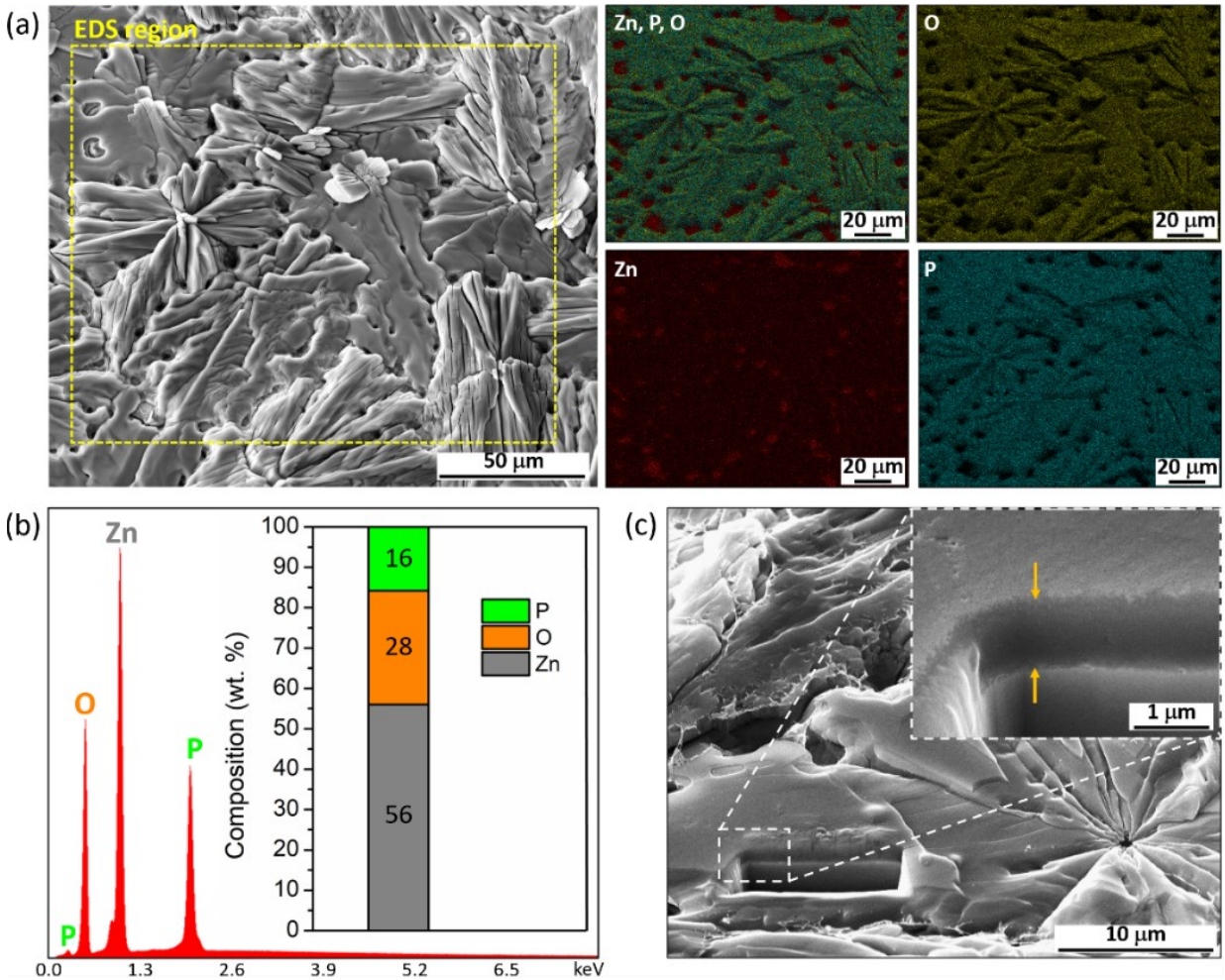

Figure 3: SE-SEM data and corresponding EDS elemental information of the ZnP coated sample: (a) SE-SEM photomicrograph of the sample surface indicating the ROI where the EDS elemental maps of Zn, P and O were collected, (b) EDS spectrum of the ROI highlighted in (a) and corresponding chemical composition, (c) SE-SEM photomicrograph of the surface, with a stage tilt of 54 º, showing a FIB cut, from which the thickness of the ZnP coating was estimated.

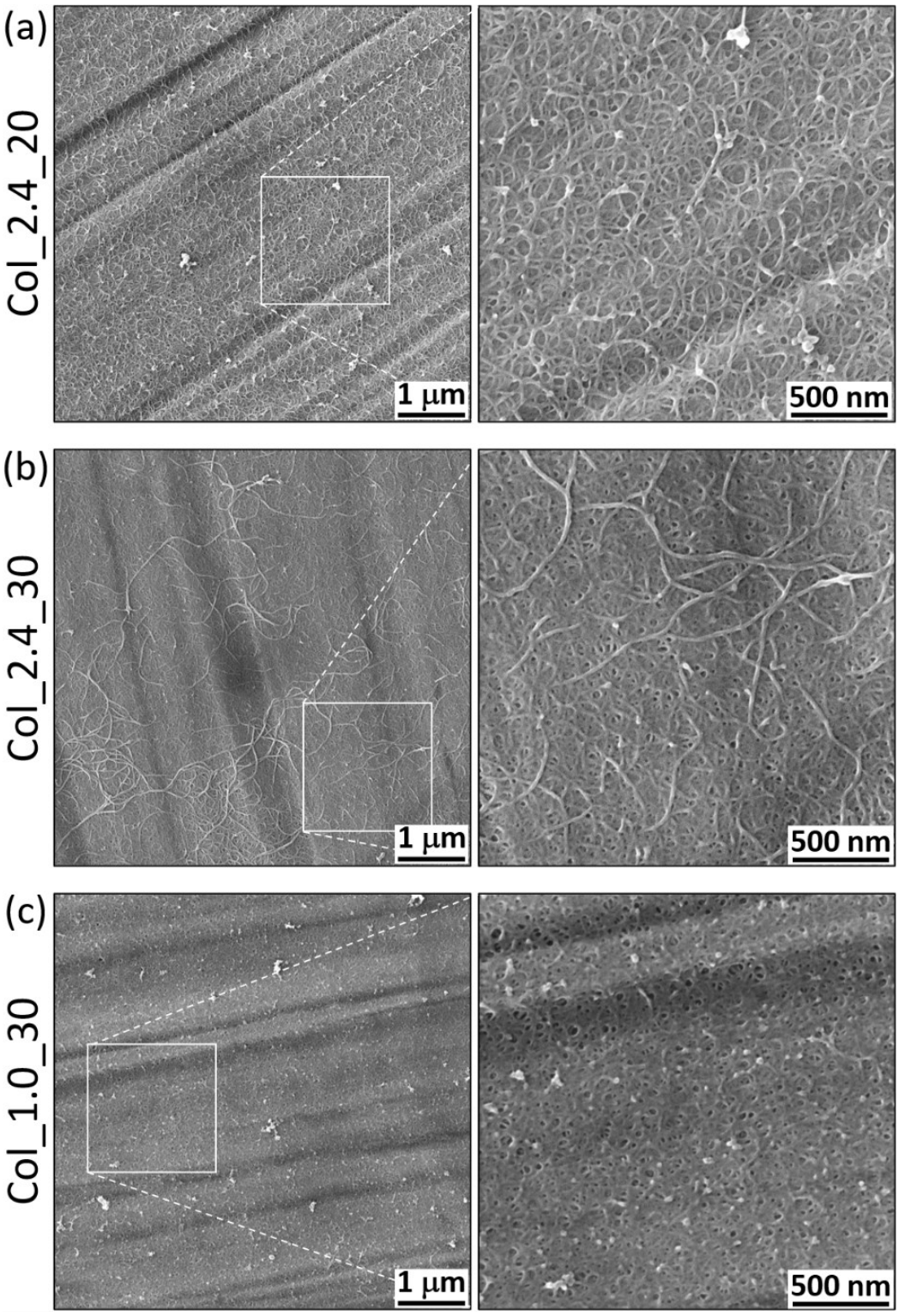

Figure 4: SE-SEM photomicrographs showing the surface morphology of the Col coatings performed by spin-coating technique on the surface of the as-homogenized Zn-3Mg alloy at 3000 rpm with different PureCol concentrations and spinning times: (a) 2.4 mg/mL and 20 s, (b) 2.4 mg/mL and 30 s, and (c) 1 mg/mL and 30 s.

3.1.3 ZnP-Col coatings

A uniform ZnP-Col coating was obtained by spin-coating the 2.4 mg/mL PureCol solution at 3000 rpm for 20 s on the already ZnP-coated sample. Figure 5 (a) shows that the Col fibrils distributed randomly and completely covered the flake-like structures of the ZnP coating, similar to those in the Zn-3Mg substrates in Figure 4 (a). In addition, the Col coating extended into the pores between the different flake-like structures, as depicted in Figure 5 (b).

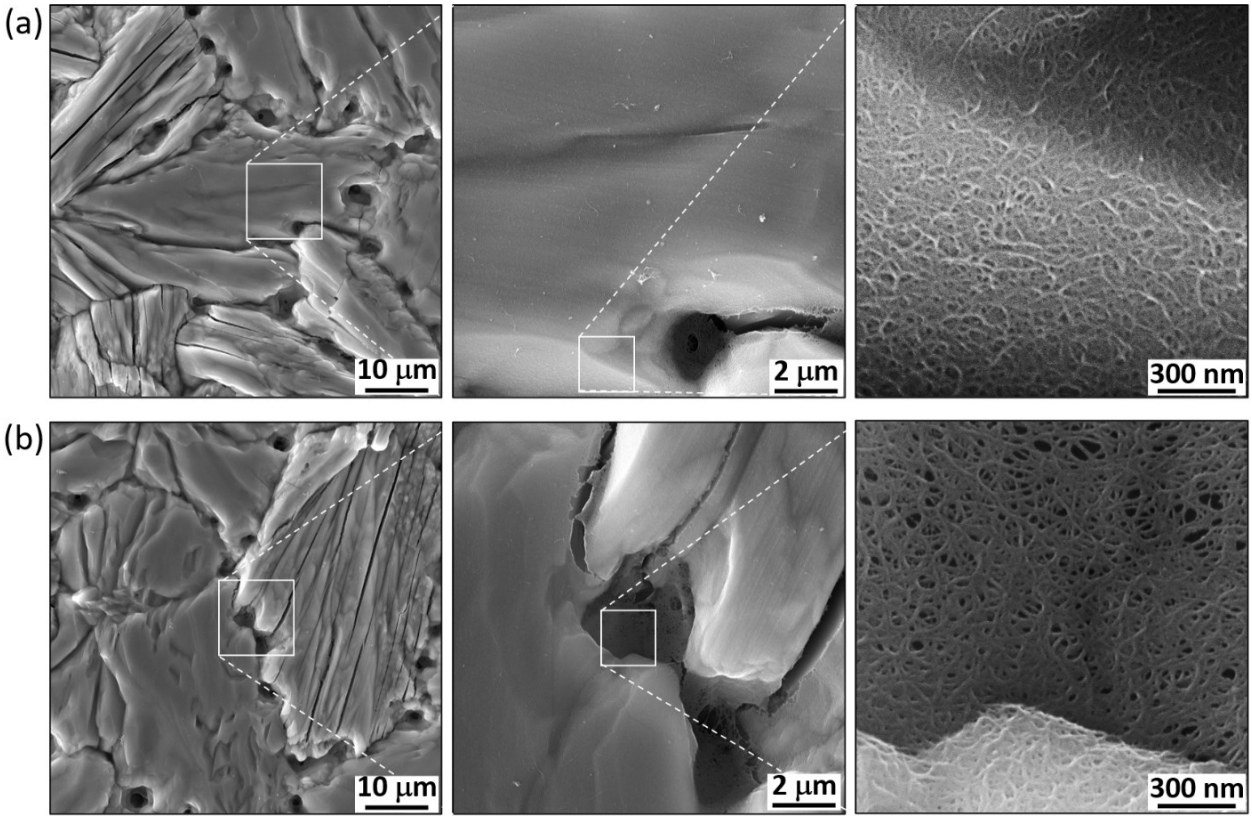

Figure 5: SE-SEM photomicrographs showing the surface morphology of the ZnP-Col coating, obtained by applying the Col_2.4_20 coating on the ZnP coated surface: (a) ROI showing uniform Col coating of the flake-like ZnP microstructure, (b) ROI showing the Col coating present in pores of the ZnP microstructure.

3.1.4 Col-AgBGN coatings

Similar to the Col-coated samples shown in Figure 4, the polishing lines of the Zn-3Mg substrate surface remained evident after spin-coating the Col-AgBGN solution at 3000 rpm for 20 s (Figure 6 (a)). Spherical nanoparticles, with diameters ranging from ~ 50-200 nm were distributed across the sample surface, as observed in Figure 6 (b). Monodispersed nanoparticles, indicated by orange arrows, generally exhibited smaller sizes compared to those highlighted by green arrows, which tended to aggregate into clusters with neighboring nanoparticles. EDS analysis of different regions in the Col-AgBGN coated samples did not identify any significant peaks corresponding to Si, the major component of AgBGN, making it challenging to estimate the composition of the observed nanoparticles using this approach.

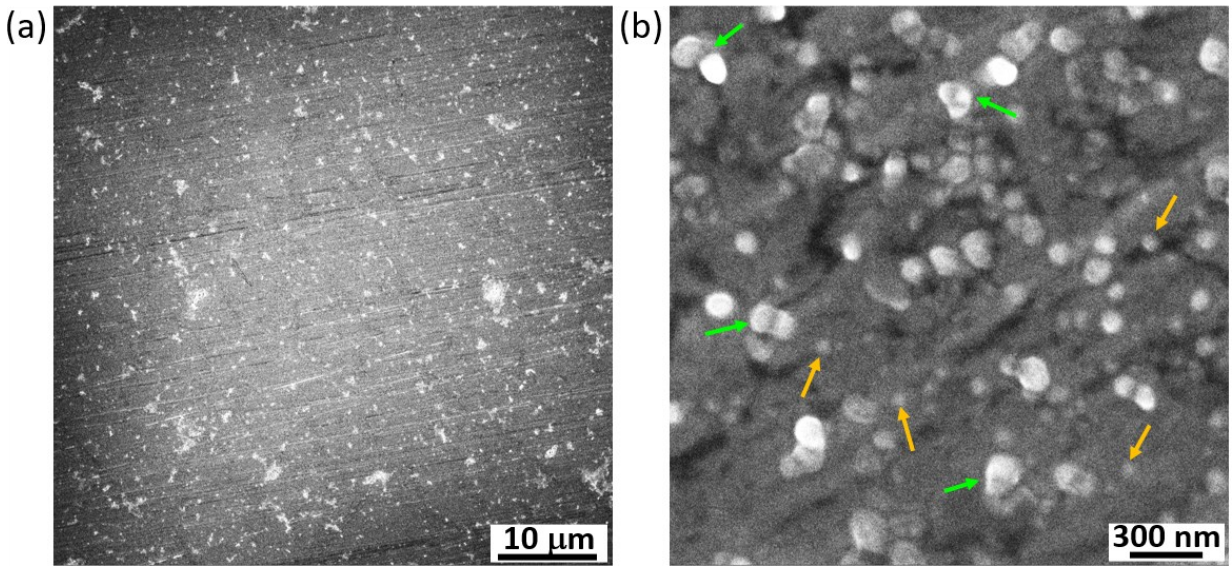

Figure 6: SE-SEM photomicrographs showing the surface morphology of the Col-AgBGN coatings obtained by spin-coating on the Zn-3Mg alloy: (a) low-magnification, (b) high-magnification, showing dispersed AgBGN of < 100 nm (orange arrows) and aggregated AgBGN clusters (green arrows).

3.2 *In vitro* degradation and corrosion resistance

The immersion degradation behavior of uncoated and ZnP-coated samples in DMEM for 6 and 21 days is depicted in Figure 7. After 6 days of immersion localized corrosion pits were observed on the Zn-rich phase of the uncoated samples (lighter phase in Figure 7 (a)). The size of these corrosion pits increased notably after 21 days immersion, leading to larger dark areas inside the Zn-rich phase (Figure 7 (b)). In contrast, the Mg_2Zn_{11} phase exhibited a more uniform corrosion during the immersion period, maintaining a similar aspect after both 6- and 21-days. The ZnP-coated samples demonstrated uniform corrosion and retained their flake-like morphology even after 21 days of immersion (Figure 7 (c) and Figure 7 (d)). In addition, newly-formed fine flakes were observed on the ZnP-coated samples immersed for 21 days, as seen in the magnified inset of Figure 7 (d).

In the uncoated samples, the amount of Zn, present in both the Zn and Mg_2Zn_{11} phases, decreased with increased immersion time at the expense of those elements forming the corrosion products (i.e., Na, C, O), as shown in Figure 7 (d). The amount of Mg in the Mg_2Zn_{11} phase remained nearly constant but the amount of O increased, suggesting the formation of additional oxide products. In the ZnP-coated samples, the Zn content also decreased with immersion time, which was counterbalanced by a slight increase in P, O, and C, and could be associated with the formation of additional fine flake-like structures, like those observed in magnified inset of Figure 7 (d).

The phase composition changes in the uncoated and ZnP-coated samples after 21 days immersion were evaluated by GIXRD (Figure 8). Diffraction peaks corresponding to zinc oxide (ZnO) and zinc hydroxide ($Zn(OH)_2$) phases were identified in the uncoated sample, along with the diffraction peaks for the Zn-rich and Mg_2Zn_{11} phases (Figure 8 (a)). In the ZnP-coated sample, diffraction peaks corresponding to a sodium zinc phosphate hydrate ($Na_2Zn(H_2PO_4) \cdot 4H_2O$) phase were identified, in addition to $Zn_3(PO_4)_2 \cdot 4H_2O$, to which most of the peaks were assigned (Figure 8 (b)). Zn and Mg_2Zn_{11} phases were also present in the ZnP-

coated sample before and after immersion. Due to overlapping diffraction angles, some peaks were assigned to multiple phases.

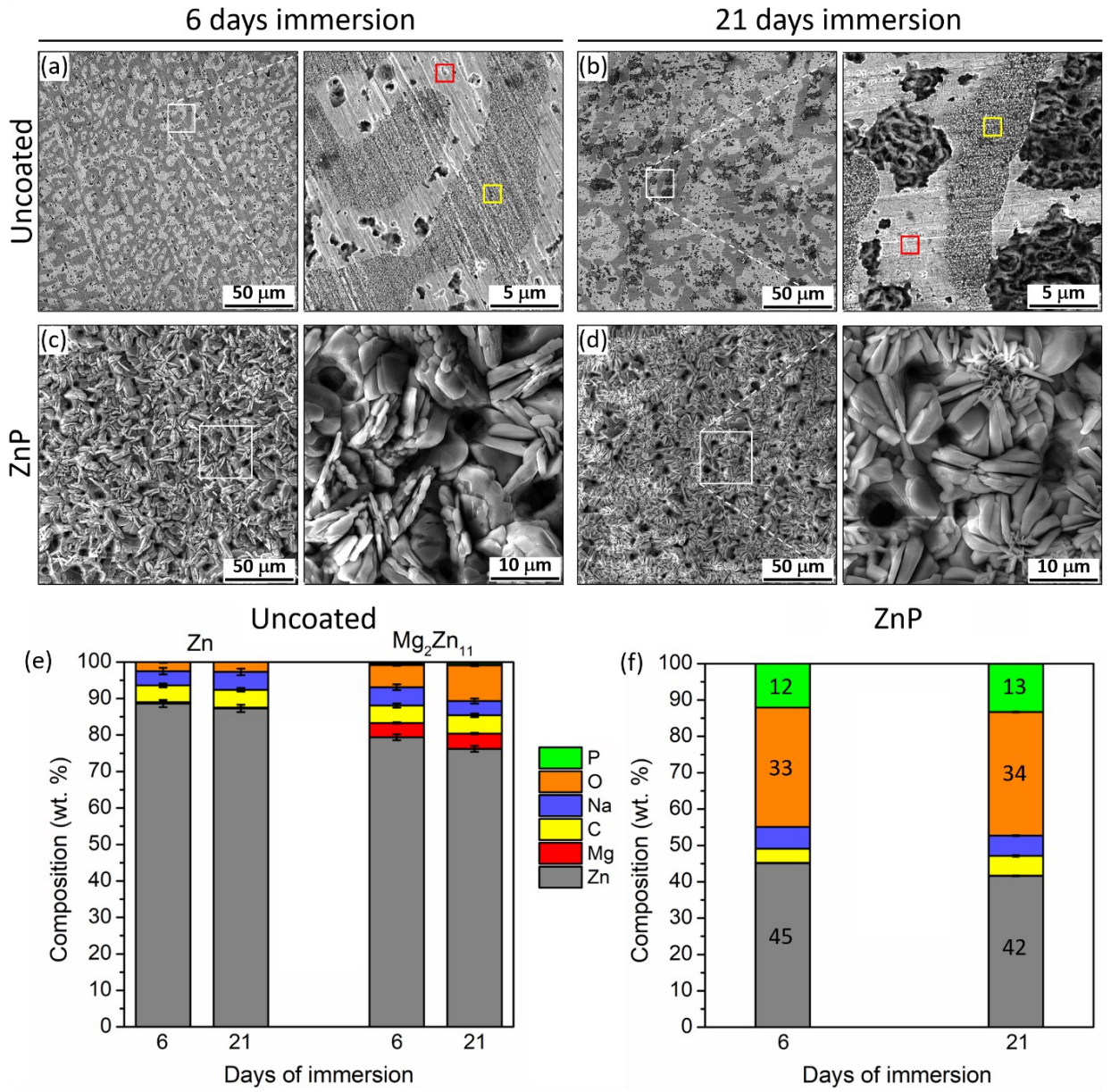

Figure 7: SE-SEM photomicrographs and EDS elemental compositions showing the *in vitro* degradation in DMEM: (a-b) uncoated samples after 6 and 21 days immersion, respectively, where the red and yellow boxes indicate the regions where EDS was performed in the Zn and Mg_2Zn_{11} phases, respectively, (c-d) ZnP coated samples after 6 and 21 days immersion, respectively; EDS elemental compositions after 6 and 21 days immersion of the (e) uncoated samples at the highlighted red and yellow boxes, and (f) ZnP coated samples at the entire regions in (c) and (d).

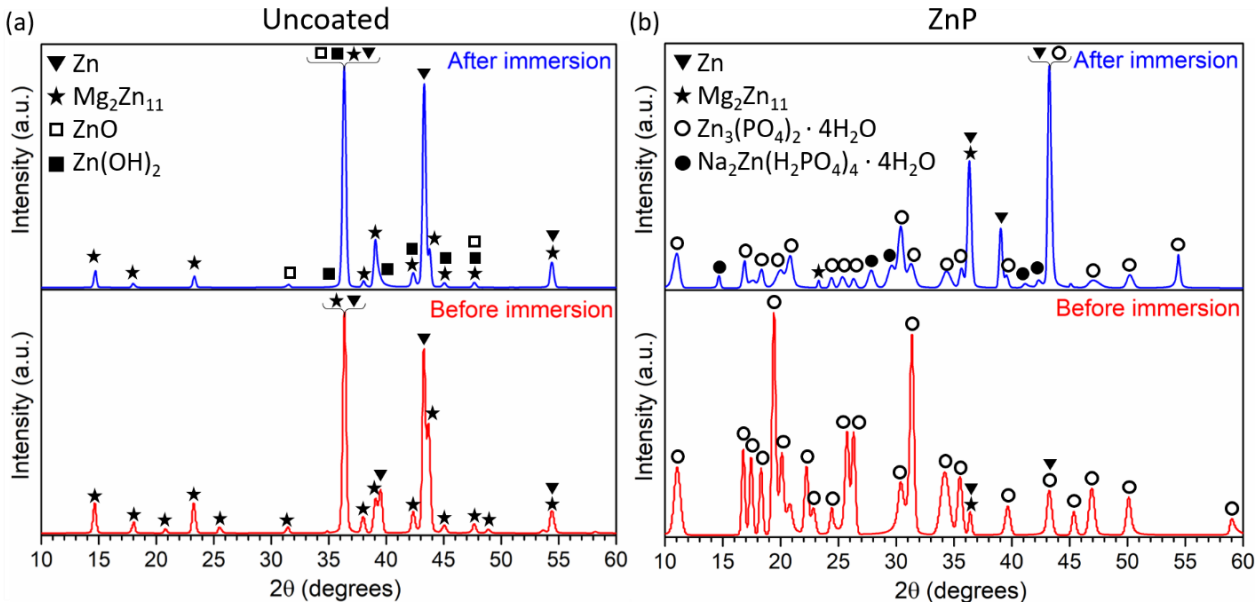

Figure 8: GIXRD scans of the (a) uncoated Zn-3Mg substrate, and (b) ZnP coated Zn-3Mg substrate, before immersion and after 21 days immersion in DMEM. Identified peaks are labeled with different symbols. Note that some peaks were attributed to several phases.

The weight loss and corrosion rate of the uncoated and ZnP-coated samples after 6, 12 and 21 days immersion in DMEM at 37 ºC are plotted in Figure 9 (a) and Figure 9 (b), respectively, and the average values are presented in Table I. The pH evolution of the immersion media, measured every other day, is represented in Figure 9 (c).

The uncoated samples exhibited slightly higher average weight loss and corrosion rate for all time points. However, due to the large standard deviation error bars, no statistical significance was found between groups. The uncoated sample reached the maximum weight loss at day 12, which was remained relatively stable until day 21, while the corrosion rate showed a similar trend until day 12, and then decreased by approximately half at day 21. In contrast, the weight loss in the ZnP-coated samples increased progressively over time, indicating a more uniform degradation rate. The corrosion rate was quite low and decreased after day 12 and remained stable until day 21. The only statistically-significant difference was observed between the corrosion rates of both samples at day 12, when that of the ZnP-coated samples was about half that of the uncoated sample.

The pH evolution of the immersion media in both samples presented similar trends (Figure 9 (c)). During the first 2 days of immersion, the pH value increased from ~ 7.4 to ~ 7.65 in both samples. Then, the pH value decreased slightly to ~ 7.55 at day 4, and was maintained reasonably stable between ~ 7.5-7.6 for the rest of the immersion test in both samples. In general, the pH was slightly larger, in the uncoated sample from day 4 to day 16, and practically the same between both samples from day 16 until the end of the immersion test at day 21.

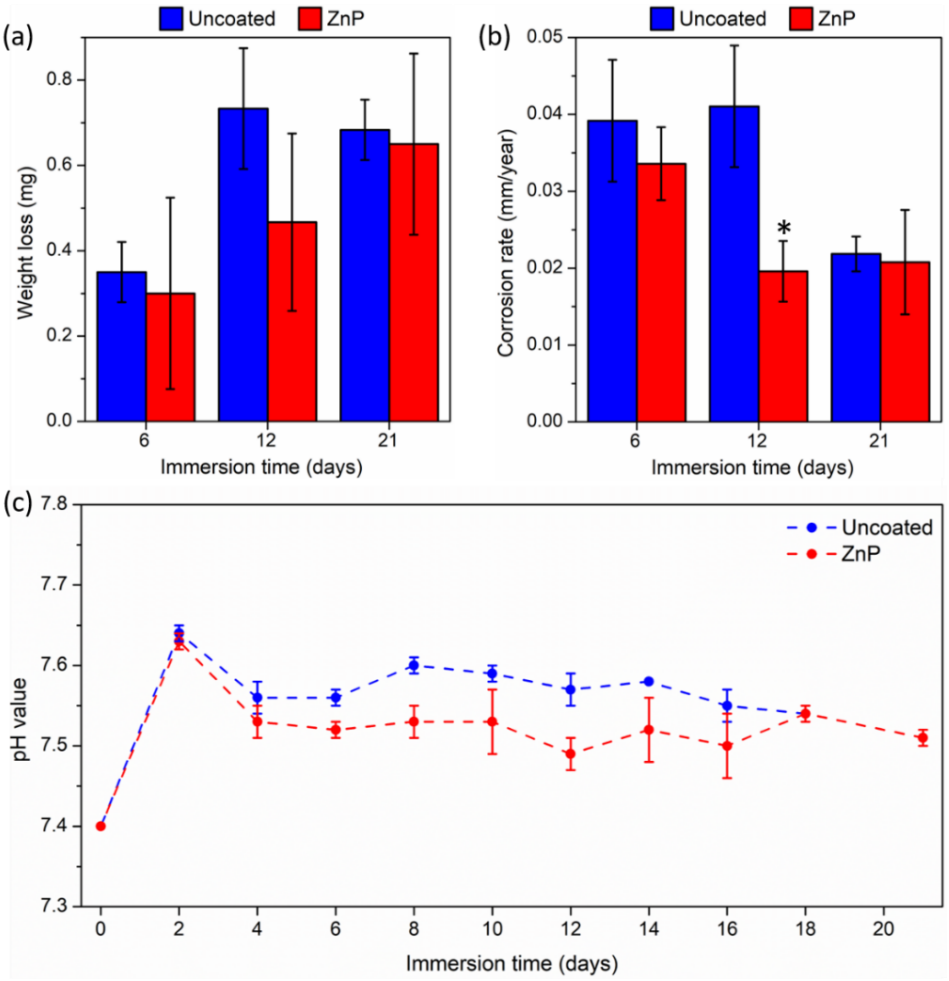

Figure 9: Evolution of the (a) weight loss, (b) corrosion rate, and (c) pH value of the uncoated and ZnP samples during the immersion test in DMEM at 37 ºC for up to 21 days. Statistical significance between groups was indicated with * for $p < 0.05$.

Table I: Average values of the weight loss and corrosion rate of the uncoated and ZnP samples estimated from the immersion test in DMEM at 37 ºC for 21 days. These values are plotted in Figure 9.

Sample	Immersion time (days)	Weight loss (mg)	Corrosion rate (mm/year)
Uncoated	6	0.350	0.0392
	12	0.733	0.0410
	21	0.683	0.0219
ZnP	6	0.300	0.0336
	12	0.467	0.0196
	21	0.650	0.0208

3.3 Indirect contact cell proliferation assay with sample extracts

3.3.1 Cytocompatibility and cell proliferation assays

The appearance of 7043L hMSC (passage 6), seeded at a density of $2.5 \cdot 10^3$ cell/cm^2, after 4- and 6-days culture in 4-fold extract dilutions (i.e., 25 % extract concentration) of uncoated, ZnP and Col-AgBGN samples are presented in Supplemental Information (Figure S1). The control group displayed star-like and spindle-like cell morphologies on day 4, while the extract groups showed increased cell density without notable morphological differences. By day 6, higher cell densities exhibited elongated shapes and aligned parallel to each other, but no significant differences in cellular morphology were observed with respect to the control groups.

Figure 10 demonstrates the cell proliferation of 7043L hMSC (passage 6) in sample extracts of different concentrations. At days 2, 4, and 6, cell numbers were significantly greater in the 6-fold and 4-fold uncoated extracts, compared to the control group. In addition, cell numbers tended to increase with extract concentration, with statistical significance observed at days 2 and 4 across all extract concentrations, and at day 6 between the highest and lowest extract concentrations. For ZnP extracts, cell numbers were significantly higher than the control at days 2, 4, and 6, except for the 6-fold extract at day 6. However, no statistical difference was found between different ZnP extract concentrations (Figure 10 (b)). Col-AgBGN extracts consistently exhibited significantly greater cell numbers than the control at days 2, 4, and 6, indicating their pronounced effect on cell proliferation and higher CCK-8 OD values (Figure 10 (c)). It is noted that only the Col-AgBGN extracts showed this trend, and that these extracts typically exhibited the highest CCK-8 OD values.

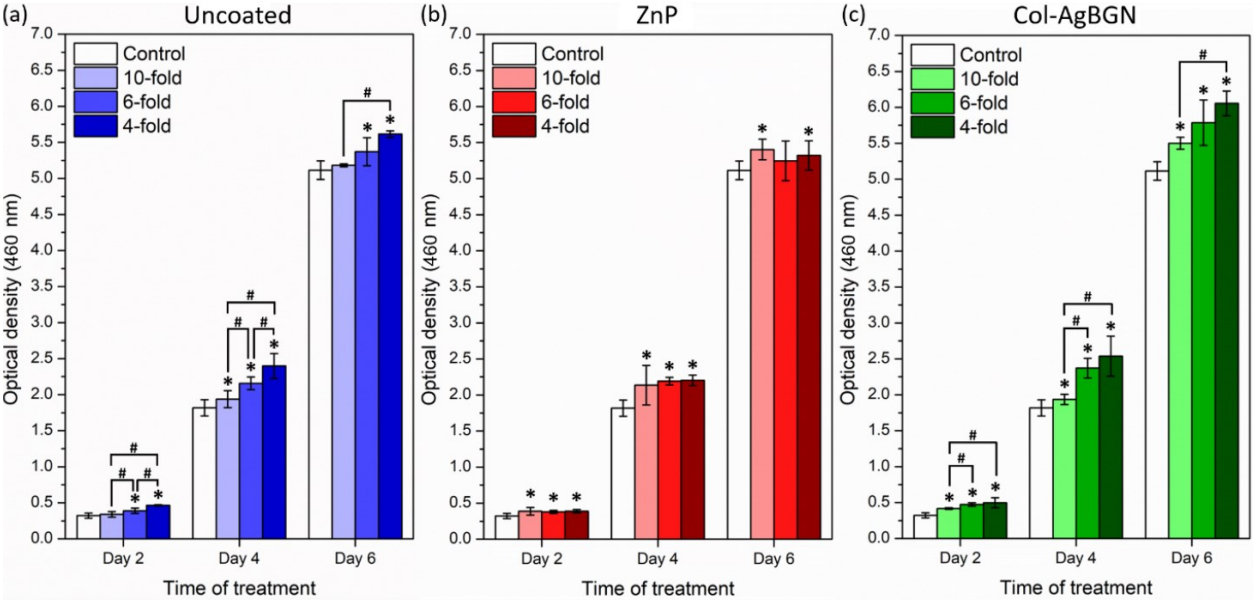

Figure 10: *In vitro* proliferation of 7043L hMSC (passage 6) measured by CCK-8 assay after 2, 4 and 6 days culture in 10-fold, 6-fold, and 4-fold extract dilutions (corresponding to 10 %, 16.7 % and 25 % extract concentration in cell culture medium, respectively) of (a) Uncoated, (b) ZnP, and (c) Col-AgBGN samples. Error bars indicate standard deviations between triplicate samples. Darker colors indicate higher extract concentrations. Statistical significance codes: * $p < 0.05$ compared with control group, # $p < 0.05$ compared between groups.

3.4 Antibacterial adhesion and viability assessment

3.4.1 Bacterial adhesion to coated surfaces

The attachment and morphology of MRSA on different samples (i.e., uncoated and coated samples) were evaluated using SEM (Figure 11). The uncoated sample, which showed the lowest surface roughness, exhibited moderate bacterial attachment, with smooth spherical surfaces indicating healthy bacteria (Figure 11 (a) inset). In general, the ZnP and ZnP-Col samples showed significantly higher bacteria attachment than uncoated sample (Figure 11 (b) and Figure 11 (c)), with slightly higher adhesion on the ZnP-Col surface. It is noted that these two samples also exhibited the largest surface areas for the bacteria to adhere to, due to the morphology of the ZnP coating. Smooth spherical and dividing bacteria were observed (green arrows). Some bacteria with anomalous morphologies were also present (red arrow), which are typically associated with damaged and/or dead bacteria.

The Col sample exhibited a granulated surface (Figure 11 (d)) and higher bacteria attachment than the uncoated sample. Like the ZnP and uncoated samples, a large number of bacteria in the Col samples appeared to be healthy, although some bacteria fragments and bacteria with distorted shapes were also observed. Lastly, the Col-AgBGN samples, with their granulated morphology (Figure 11 (e)), had fewer adherent bacteria, mostly fragmented or with anomalous morphologies.

It is important to emphasize that SEM imaging provided information about the morphology and density of bacteria adhered to the samples, but the bacteria viability assessment on the material surface requires additional methods like fluorescent CLSM.

3.4.2 Viability of bacteria adhered to coated surfaces

The viability of bacteria adhered to sample surfaces was evaluated after 7 days of incubation in a bacterial suspension of 10^7 CFU/mL in TSB. Viability was assessed by analyzing representative fluorescence CLSM images obtained from live/dead staining (Figure 12). Bacteria appeared as fine fluorescent points or larger fluorescent areas indicating individual bacteria dispersed in the sample (Figure 12 (a) and Figure 12 (d)) or bacterial colonies (Figure 12 (b) and Figure 12 (e)), respectively.

Coated samples exhibited similar ratios of green and red pixels, with a majority of green pixels indicating live bacteria. However, the Col-AgBGN sample (Figure 12 (e)) had a significantly higher number of red pixels, suggesting a greater presence of dead bacteria.

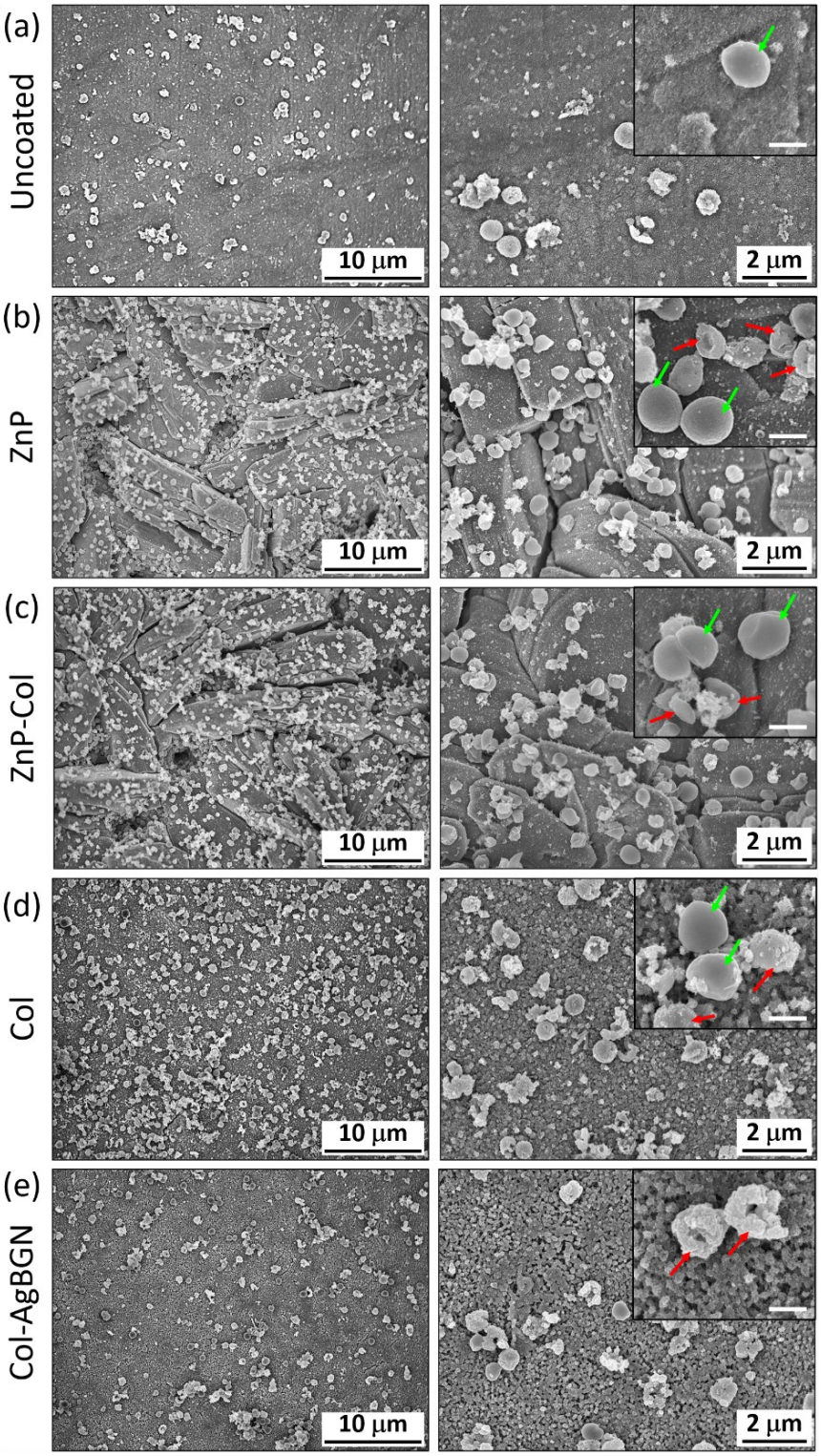

Figure 11: SE-SEM photomicrographs showing MRSA adhesion to the surface of the Zn-3Mg alloy samples with different coatings, after 7 days incubation in an initial bacteria suspension of 10^7 CFU/mL in TSB: (a) Uncoated, (b) ZnP, (c) ZnP-Col, (d) Col, and (e) Col-AgBGN. The insets at the top-right corners of the higher magnification images show examples of live bacteria (green arrows) and dead bacteria (red arrows). The scale bar in the insets represents 500 nm.

The live/dead percentages were similar between the uncoated, ZnP-Col, and Col samples, with approximately 76%, 75%, and 71% of live bacteria, respectively (Figure 13). The ZnP sample showed a lower percentage of live bacteria (approximately 65%), representing a 10% decrease compared to the uncoated sample. In contrast, the Col-AgBGN sample exhibited a significant reduction in bacteria viability, with an average of 31% live bacteria, indicating a pronounced antibacterial effect.

Table II presents the estimated bacteria density attached to the samples, the live/dead bacteria percentages, and the live bacteria density for the different samples. The uncoated and Col-AgBGN samples exhibited similar bacteria densities between 250-270·10^3 bacteria/mm^2, while the ZnP-Col and Col samples had comparable bacteria densities between 630-650·10^3 bacteria/mm^2. The ZnP sample showed lower bacteria density than the ZnP-Col and Col samples, but the bacteria density was approximately twice as high as the uncoated and Col-AgBGN samples. Despite the comparable densities of bacteria in the uncoated and Col-AgBGN samples, the live bacteria density in the Col-AgBGN sample was approximately 60% lower than that of the uncoated sample. This difference can be attributed to a significantly higher percentage of dead bacteria in the Col-AgBGN sample. Overall, the ZnP-Col and Col samples exhibited the highest live bacteria densities, followed by ZnP, uncoated, and Col-AgBGN samples.

Table II: Quantification of the total bacteria density, live/dead bacteria percentages, and live bacteria density adhered to the sample surfaces, estimated from the analysis of the color pixel counts from fluorescent CLSM images.

Sample	Bacteria density (bacteria/mm^2) ·10^3	Live bacteria (%)	Dead bacteria (%)	Live bacteria density (bacteria/mm^2) ·10^3
Uncoated	254	76	24	193
ZnP	522	65	35	339
ZnP-Col	636	75	25	477
Col	652	71	29	463
Col-AgBGN	266	31	69	82

3.4.3 Viability of bacteria in suspension

To evaluate bacterial viability over time, an initial bacterial suspension of 10^7 CFU/mL in TSB was cultured with different samples (coated and uncoated) for 7 days. The OD values were taken at multiple time points (Figure 14) to evaluate the bacterial density. This testing procedure ensured maintaining bacteria in suspension. The bacterial viability in the untreated group (i.e., no sample) was significantly higher than that of all the other groups, for all the time points (Figure 14 (a)). The concentration of planktonic bacteria increased over time for all groups except for the uncoated group, which remained relatively constant (Figure 14 (b)).

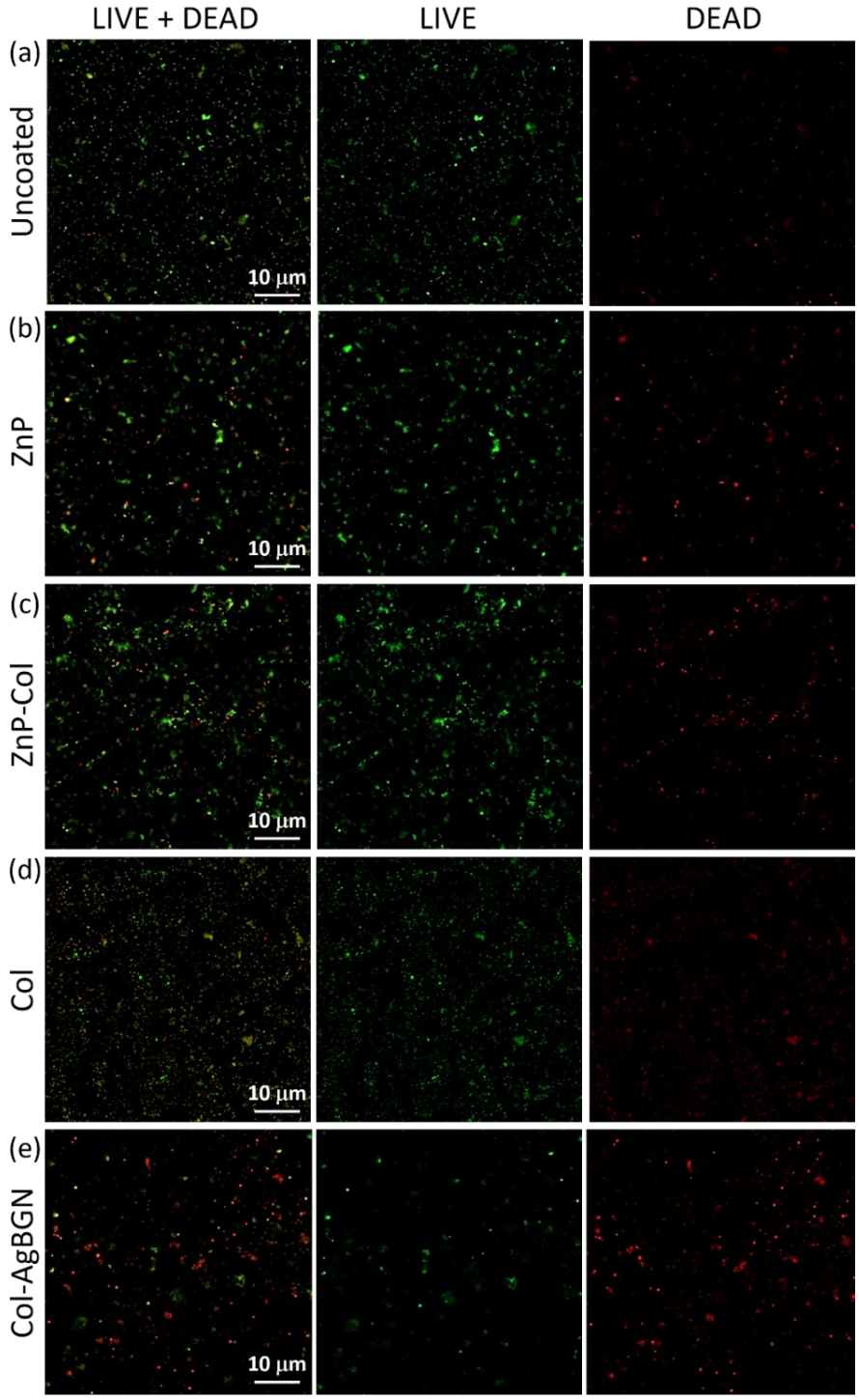

Figure 12: CLSM images showing MRSA viability on the surface of the Zn-3Mg alloy samples with different coatings, after 7 days incubation in an initial bacteria suspension of 10^7 CFU/mL in TSB: (a) Uncoated, (b) ZnP, (c) ZnP-Col, (d) Col, and (e) Col-AgBGN. SYTO 9 and propidium iodide stains were used to stain intact membranes and damaged membranes with fluorescent green and red, respectively. Images in "LIVE + DEAD" column shows green and red fluorescence, images in "LIVE" column show only green fluorescence, and images in "DEAD" column show only red fluorescence.

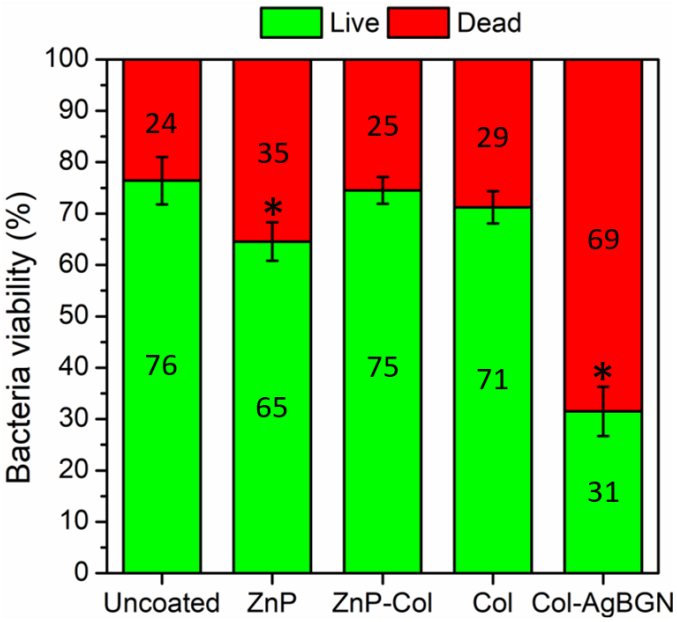

Figure 13: Quantification of live and dead MRSA on the surface of the Zn-3Mg alloy samples with different coatings, after 7 days incubation in an initial bacteria suspension of 10^7 CFU/mL in TSB. The percentages of live and dead bacteria were calculated from the number of green and red pixels in triplicate CLSM images, using a pixel color counter plugin for ImageJ. The error bars indicate the standard deviations between triplicate samples. The numbers inside the green and red bars indicate the average live and dead percentages of MRSA calculated for each sample, respectively. Statistically significance code: * $p < 0.05$ compared with uncoated group.

In general, the concentration of planktonic bacteria increased over time most of the groups, except for the uncoated group. The concentration of planktonic bacteria in the uncoated group remained relatively constant at OD ~ 0.6 until day 3, after which it decreased to OD ~ 0.4 at day 5 and maintained that level until day 7 (Figure 14 (c)). Both ZnP and ZnP-Col groups showed similar trends, with the concentration of planktonic bacteria decreasing to OD ~ 0.4-0.5 on day 3, and gradually increasing to OD ~ 0.8 on day 7 (Figure 14 (d) and Figure 14 (e), respectively). In the Col group, the concentration of planktonic bacteria decreased to OD ~ 0.4 on day 2, then, increased up to OD ~ 0.6 on day 5, and remained constant until day 7 (Figure 14 (f)). Interestingly, the Col-AgBGN group (Figure 14 (g)) showed a progressive increase in the concentration of planktonic bacteria, reaching OD ~ 1.1 on day 5, and maintaining a similar level on day 7. Notably, among the coated samples, the Col-AgBGN group was the only one that consistently exhibited an increase in planktonic bacteria concentration in the solution.

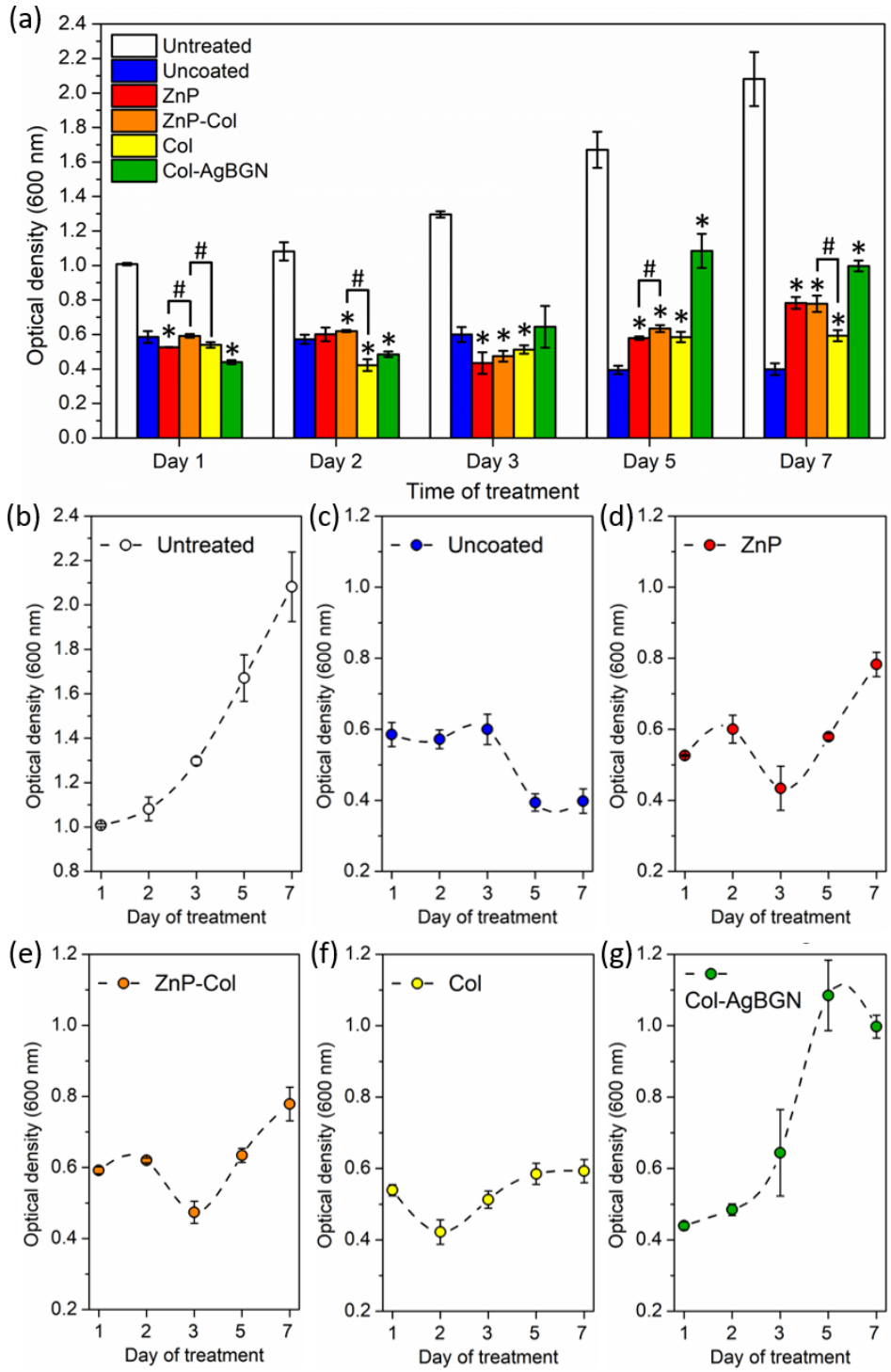

Figure 14: Assessment of MRSA suspension viability, with an initial concentration of 10^7 CFU/mL in TSB, after 1, 2, 3, 5, and 7 days incubation with Zn-3Mg alloy samples having different coatings. (a) comparative plot with the OD values for all samples and time points. (b-g) Individual plots showing the evolution of the OD values for each sample over time. Untreated refers to a MRSA suspension incubated with no sample. Error bars indicate standard deviations between triplicate samples. Statistical significance codes: * $p < 0.05$ compared with Uncoated group, # $p < 0.05$ compared between groups.

4 DISCUSSION

Zinc and Zn-based alloys have shown promise for bone and vascular implant applications [41]. The rapid degradation of Zn-based implants could lead to systemic toxicity, emphasizing the need to control Zn^{2+} release. Coatings are an effective strategy to modulate the degradation rate and tailor the performance for specific medical needs. In this study, four different coatings were evaluated to understand their potential to reduce corrosion and improve biocompatibility for safe biomedical applications.

4.1 Formation of the zinc phosphate coating

A chemical conversion protocol, based on the work of Su *et al.* [22], was successfully applied to Zn-3Mg alloys, resulting in a distinctive flake-like appearance with a uniform pore distribution (Figure 2 (c) and Figure 2 (d)). The chemical composition analysis confirmed the presence of hopeite in the ZnP coating, (Figure 3 (b)). The flower-like structures observed in Figure 3 were consistent with ZnP-coated AZ91D Mg alloy [42], and attributed to the nucleation sites of hopeite (i.e., zinc phosphate tetrahydrate) crystals.

The growth mechanism of the ZnP coatings can be described in two stages. During the initial 3 minutes of immersion in the ZnP solution, numerous hopeite crystals nucleated and grew uniformly across the substrate, forming a distinctive flower-like structure that gradually covered the entire sample. In the second stage, these structures interacted and continued to grow vertically, resulting in the characteristic flake-like structure observed after 5 minutes of immersion. Therefore, the coating structure can be manipulated by the immersion time. The understanding of this growth process provides valuable insights mechanisms governing the ZnP coating morphology.

4.2 Formation of the collagen-based coatings

Among the three different collagen coatings presented in Figure 4, the one obtained with 2.4 mg/mL PureCol by spin-coating for 20 s at 3000 rpm resulted in a well-defined assembly of Col fibrils, with a fibril thickness congruent with other Col coated samples [43,44]. Increasing the spin-coating time by 10 s (Figure 4 (b)) led to a decrease in the number of Col fibrils attached to the surface, indicating that the centripetal force pulled more fibrils away from the rotation axis. A thin porous layer of Col was noticeable beneath the Col fibrils. On the other hand, decreasing the PureCol concentration to 1 mg/mL resulted in a porous Col coating without Col fibrils (Figure 4 (c)). A concentration of 2.4 mg/mL PureCol is recommended for gel formation, and a lower concentration might not be sufficient for Col fibril formation during incubation.

The formation of the ZnP-Col coating involved spin-coating the selected Col solution onto the ZnP-coated substrate, resulting in complete coverage of the flake-like ZnP surface by Col fibrils (Figure 5). While dual coatings combining calcium phosphate and collagen have been reported for improved biocompatibility and cell adhesion [45,46], no previous literature mentioned the specific ZnP-Col coating synthesized in this study.

A uniform Col-AgBGN coating was achieved, with dispersed nanoparticles observed across the substrate surface. From Figure 6, it was evident that monodispersed nanoparticles below 50 nm in diameter and nanoparticle aggregates ranging from approximately 100-200 nm were present. Although elemental analysis could not determine the nature of these nanoparticles, due to their low concentration and interference from the substrates, the *in vitro* performance of the Col-AgBGN coatings (Figure 10) provided support for their identification as AgBGNs. Aggregation of AgBGNs is a common phenomenon driven by surface energy reduction [47,48]. To minimize aggregation, PEG was utilized in the Col-AgBGN coating process to lower the surface charge of the AgBGNs. It is worth noting that centrifugation of the AgBGN-PEG solution, before replacing the supernatant with the 2.4 mg/mL PureCol solution for Col-AgBGN

formation, might have contributed to AgBGN aggregation. Another possible factor could be the spin-coating technique, as the collagen matrix could serve as an adhesive, holding a small concentration of AgBGNs in place. During spin-coating, loosely bonded AgBGNs may migrate towards the sample edges under the centripetal force and encounter firmly bound sets of AgBGNs within the matrix, resulting in the observed nanoparticle aggregates.

4.3 Enhanced corrosion behavior of zinc phosphate coating

The degradation behavior of absorbable metals is crucial as it affects the ion release and pH evolution, which in turn influences the cellular response at the implantation site. Figure 7 revealed different corrosion behaviors between the Zn and Mg_2Zn_{11} phases. The Zn phase exhibited corrosion pits that increased in size with increased immersion time, while the Mg_2Zn_{11} phase showed a more uniform granulated topography. EDS analysis confirmed the presence of the corrosion products, ZnO and $Zn(OH)_2$, with higher concentrations of the Mg_2Zn_{11} phase. Weight loss measurements indicated a relatively uniform corrosion rate of around 0.04 mm/year from 6 to 12 days immersion, which is similar to that reported (~ 0.03 mm/year) from an immersion test of pure Zn in SBF for 10 days [49]. The pH value remained stable within the physiological range during the initial 12 days of immersion, in agreement with the trends observed for other Zn-based alloys [50].

The ZnP coating showed minimal changes in morphology during immersion, with the flake-like microstructure remaining intact. Fine flakes, evenly distributed across the microstructure, were observed, potentially associated with Na-containing corrosion products. Carbon (C) was detected in all samples, likely originating from degradation products of the DMEM media [51]. As a result of the corrosion process, the thickness of the ZnP coating is expected to decrease, and this might be related to the increased peak intensity of the Zn-rich and Mg_2Zn_{11} phases from the substrate in the GIXRD spectrum after 21 days immersion.

The ZnP coating exhibited slower and more uniform degradation compared to the uncoated samples. Corrosion rate calculations and weight loss measurements supported this observation and were consistent with the enhanced corrosion resistance of ZnP coatings compared to pure Zn [22]. The release of Zn ions from the ZnP coated samples was lower than that from pure Zn, suggesting a controlled degradation process. pH values of the ZnP samples remained similar to those of pure Zn [22], indicating no significant differences. It should be noted that the combined degradation of the substrate and coating is associated with the release of hydrogen gas into the surrounding medium. This may lead to the formation of detrimental gas pockets around the implant, hindering a fully accommodation of the tissue around implant and advancing implant loosening and/or potential failure [52–55]. To this end, the study of hydrogen evolution during the corrosion process is a key parameter to be monitored in absorbable metal applications, and although it was out of the scope of this study, it should be considered in a follow-up study.

4.4 Enhanced cytocompatibility of bioglass nanoparticle-based coating

The indirect proliferation assay with sample extracts was performed up to 7 days to ensure non-confluence of control groups. Increasing extract concentrations led to gradual increases in cell viability for uncoated and Col-AgBGN extracts, while no such trend was observed for ZnP extracts. The enhanced cell proliferation may be attributed to the presence of degradation products and released ionic species. Even though the pH and ionic concentration was not monitored on the extracts, the lack of cytotoxicity suggests both indicators were within the physiological range. Notably, the uncoated extracts exhibited enhanced cell viability consistent with previous findings [11]. However, in contrast to Murni's study[11], a significant decrease in cell viability on day 7 was not observed, suggesting better control of non-toxic concentration release from bulk samples compared to their powder structure. In contrast, the ZnP extracts consistently exhibited

cell viability regardless of concentration, contradicting the concentration effect observed by Su *et al.* [22] for endothelial and pre-osteoblast cells. Col-AgBGN extracts showed significantly higher cell viabilities than the control, with the 4-fold extract displaying the greatest cytocompatibility among all groups. The release of Si^{2+}, Ca^{2+}, and Ag^{+} ions, debris particles from AgBGNs [29], and nutrients from Collagen Type I from Col-AgBGN degradation likely contributed to enhanced cell viability.

The released Ag^{+} ions during AgBGN degradation and their interaction with Zn^{2+} did not have any harmful cytotoxic effects. This is consistent with the findings of Li *et al.* [56], who showed that fibroblasts and osteoblasts cultured in Zn-4Ag alloy extracts exhibited similar viabilities to that for the Ag-free control samples, with no significant differences compared to pure Zn samples.

Furthermore, the degradation of Col in the Col-AgBGN coating may have contributed to the observed increase in cell viability. Col is commonly used as a coating material to enhance cell adhesion and tissue integration during implantation. However, in our indirect proliferation test, cells were not in direct contact with the Col-AgBGN coated sample, suggesting that the degradation products of Col may not have played a critical role in cell proliferation. This is supported by previous studies that have shown that despite improved cell adhesion, osteoblasts do not exhibit accelerated proliferation on Col-coated substrates [57–59]

4.5 Antibacterial activity of bioglass nanoparticle-based coating

The coated samples were also evaluated for their antibacterial behavior against MRSA colonization. Bacterial adhesion is key for the implant as was previously explained in the "race for the surface" phenomenon. SEM analysis (Figure 11) and CLSM imaging (Figure 12) showed low bacterial adhesion on the uncoated and Col-AgBGN samples, while the ZnP, ZnP-Col, and Col samples had higher bacterial numbers. The lower bacteria adhesion on uncoated samples observed in the SEM analysis may be due to a smoother surface causing bacteria to be washed out during sample preparation. It is hypothesized that the uncoated sample had more loosely attached bacteria, as supported by the decrease in planktonic bacteria in OD measurements, indicating an increase in bacteria attached to the sample surface.

The higher bacterial colonization in ZnP and ZnP-Col samples may be attributed to their higher microscopic roughness, as reported in previous studies [60–62]. Our findings suggest that bacteria remaining after 1 day of exposure to ZnP and ZnP-Col samples can proliferate and colonize the surface by day 7, which explains the high bacteria density seen in Figure 11. The increase in OD_{600} value may be attributed to bacteria reaching a high density on the ZnP and ZnP-Col surface after 3 days, resulting in new bacteria being released into the suspension rather than staying attached to the sample surface, similar to biofilm formation [63]. The Col sample exhibited surface roughness, possibly due to collagen degradation products, yet it was smoother than that for the ZnP-containing coatings.

Due to the natural origin of collagen, as well as its fibrillar assembly in the synthesized coatings, it is reasonable to believe that collagen can also enhance bacteria attachment [64]. Therefore, the increase in OD_{600} for Col samples may follow a comparable process than that of the ZnP-containing coatings. Despite similar surface topography, the Col-AgBGN sample showed significantly lower bacteria viability after 7 days compared to other samples. The interpretation of the bacteria evolution in Col-AgBGN may differ from other coatings. Gradual OD increase (Figure 14) suggests decreasing bacteria density on the sample surface over time. Live/dead staining and CLSM imaging (Figure 12) showed similar ratios for most samples except Col-AgBGN. Quantified bacterial viability (Figure 13) revealed comparable percentages for ZnP-Col, Col, and uncoated samples (75%, 71%, and 76% respectively). ZnP exhibited significantly lower bacterial viability (65%) than the uncoated sample, supporting antibacterial effects reported by Su *et al.* [22].

The SEM photomicrographs (Figure 11) also revealed comparable bacterial attachment on the uncoated and Col-AgBGN samples. However, the viability of bacteria on the uncoated sample (76%) was significantly higher than in the Col-AgBGN coated sample (31%). The Col-AgBGN coating demonstrated superior bactericidal activity, as indicated by the substantial reduction in live bacteria. The proposed antibacterial mechanism (Figure 15) involves stages:

- Stage I (Figure 15 (a)): Time 0 of the exposure. The fibrillar collagen matrix maintains the AgBGN attached to the sample surface, and bacteria remain in suspension.
- Stage II (Figure 15 (b)): Degradation of the matrix. Release of AgBGN retained by Col fibrils. There is bacterial proliferation and deposition in the coating.
- Stage III (Figure 15 (c)): Degradation of AgBGN. Release of ionic species[65] creating a toxic environment surrounding the AgBGN, whether in suspension or attached to the collagen matrix. A number of mechanisms (Ag^+, osmotic effect, nanoparticle debris and reactive oxygen species) lead to the antibacterial effect of the nanoparticles, as reported previously [66].

The granulated surface of MRSA (Figure 11 (e)) may be attributed to the extracellular debris resulting from bacteria lysis [67,68]. In addition, membrane disruption is suggested from the presence of cell-wall fragments, potentially caused by nanosized particles penetrating MRSA [30].

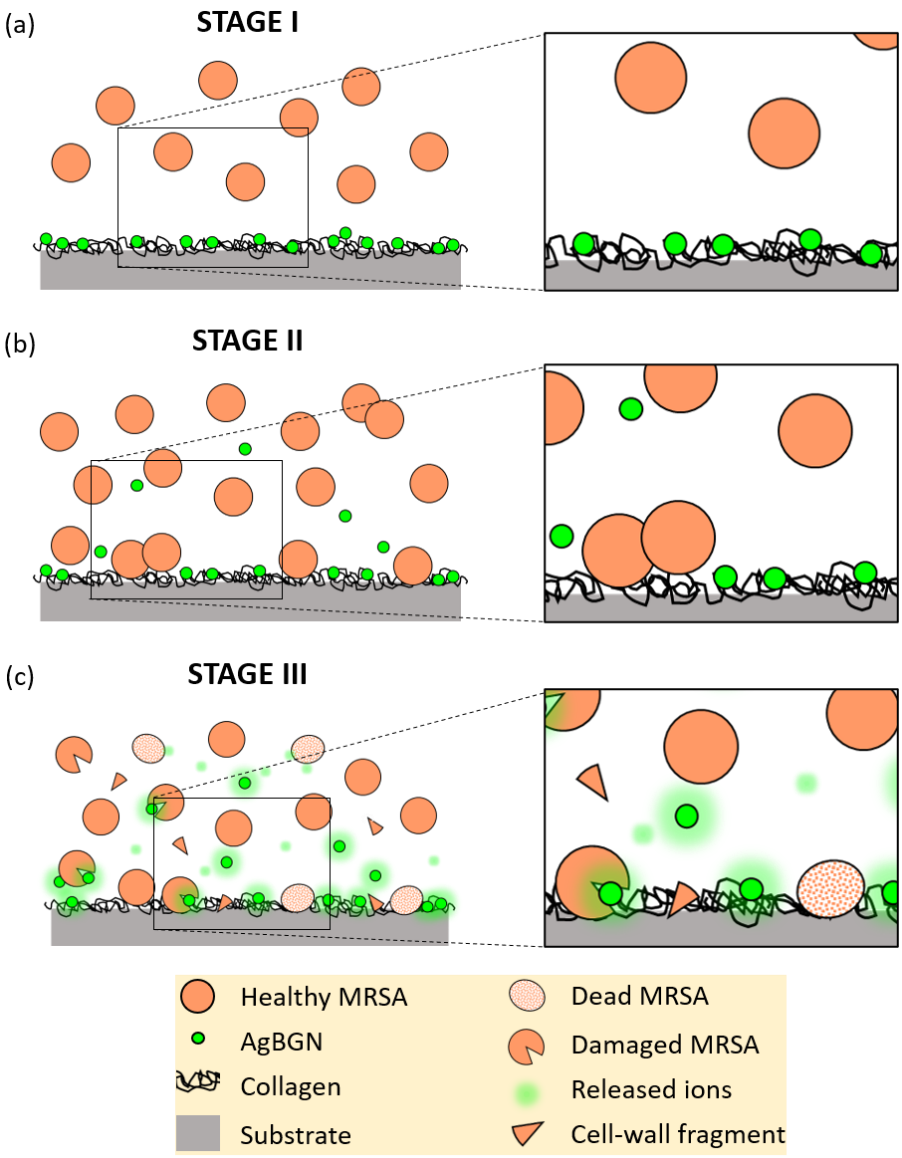

Figure 15: Scheme of the antibacterial mechanism proposed for the Col-AgBGN coatings in the Zn-3Mg alloy substrate.

5 SUMMARY AND CONCLUSIONS

This study successfully developed biodegradable coatings (ZnP, ZnP-Col, Col, and Col-AgBGN) on a Zn-3Mg alloy substrate for potential biomedical applications. The coatings were synthesized using different methods, showcasing the versatility of the fabrication process.

A uniform corrosion behavior was achieved for the ZnP-containing coatings, which also exhibited controlled weight loss over time, making it a promising protective barrier for the substrate. Additionally, improved biocompatibility was demonstrated by means of increased cell viability after exposure to extracts of all coated samples. Notably, the Col-AgBGN extracts exhibited the highest cytocompatibility, due to the release of ionic species (i.e., Si^{2+} and Ca^{2+}) from the AgBGN degradation.

The rougher surface topography in ZnP-containing samples, as well as the nutrient-rich matrix of the Col-containing samples was favorable for bacterial attachments. Nonetheless, the presence of AgBGN in Col-AgBGN coatings significantly lowered the bacterial viability. In fact, the antibacterial mechanism of Col-AgBGN coatings involved combined effects (i.e., Ag^{+} ion release, nanoparticle debris, etc) that induce damage in bacterial cell envelopes beyond repair.

Overall, the synthesized coatings demonstrated remarkable corrosion resistance, biocompatibility, and antibacterial properties, making them potential candidates for absorbable biomedical devices. Further research can involve exploring the interaction of coatings and host tissue as well as assessing their mechanical properties and durability to meet the demands of service life. The current findings indicate that these coatings have the potential to elevate the performance and safety of biomedical implants by controlling corrosion, promoting cell viability, and combating bacterial colonization.

6 ACKNOWLEDGMENTS

The authors would like to acknowledge Professor Megumi Kawasaki and Dr. J.-K. Han of Oregon State University for processing the alloys studied. The funding for this research was partially supported by the National Science Foundation Division of Material Research, under Grant No. DMR-1607942 through the Metals and Metallic Nanostructures (MMN) program (DHE & CJB).

Supporting Information: Additional experimental details, materials, and methods, including photographs of experimental setup.

7 BIBLIOGRAPHY

(1) Grainger, D. W. The Williams Dictionary of Biomaterials. *Mater. Today* **1999**. https://doi.org/10.1016/s1369-7021(99)80066-2.

(2) Katarivas Levy, G.; Goldman, J.; Aghion, E. The Prospects of Zinc as a Structural Material for Biodegradable Implants—A Review Paper. *Metals (Basel).* **2017**, *7* (10), 402. https://doi.org/10.3390/met7100402.

(3) Niinomi, M.; Nakai, M. Titanium-Based Biomaterials for Preventing Stress Shielding between Implant Devices and Bone. *International Journal of Biomaterials*. 2011. https://doi.org/10.1155/2011/836587.

(4) Piao, C.; Wu, D.; Luo, M.; Ma, H. Stress Shielding Effects of Two Prosthetic Groups after Total Hip Joint Simulation Replacement. *J. Orthop. Surg. Res.* **2014**. https://doi.org/10.1186/s13018-014-0071-x.

(5) Witte, F.; Eliezer, A. Biodegradable Metals. In *Degradation of Implant Materials*; 2012. https://doi.org/10.1007/978-1-4614-3942-4_5.

(6) Hermawan, H. Updates on the Research and Development of Absorbable Metals for Biomedical Applications. *Prog. Biomater.* https://doi.org/10.1007/s40204-018-0091-4.

(7) Vojtěch, D.; Kubásek, J.; Šerák, J.; Novák, P. Mechanical and Corrosion Properties of Newly Developed Biodegradable Zn-Based Alloys for Bone Fixation. *Acta Biomater.* **2011**. https://doi.org/10.1016/j.actbio.2011.05.008.

(8) Plum, L. M.; Rink, L.; Haase, H. The Essential Toxin: Impact of Zinc on Human Health. *Int. J. Environ. Res. Public Health* **2010**, *7* (4), 1342–1365. https://doi.org/10.3390/ijerph7041342.

(9) Brown, K. H.; Peerson, J. M.; Rivera, J.; Allen, L. H. Effect of Supplemental Zinc on the Growth and Serum Zinc Concentrations of Prepubertal Children: A Meta-Analysis of Randomized Controlled Trials. *Am. J. Clin. Nutr.* **2002**, *75* (6), 1062–1071. https://doi.org/10.1093/ajcn/75.6.1062.

(10) International Zinc Nutrition Consultative Group (IZiNCG); Brown, K. H.; Rivera, J. A.; Bhutta, Z.; Gibson, R. S.; King, J. C.; Lönnerdal, B.; Ruel, M. T.; Sandtröm, B.; Wasantwisut, E.; et al. International Zinc Nutrition Consultative Group (IZiNCG) Technical Document #1. Assessment of the Risk of Zinc Deficiency in Populations and Options for Its Control. *Food Nutr. Bull.* **2004**, *25* (1 Suppl 2), S99-203.

(11) Murni, N. S.; Dambatta, M. S.; Yeap, S. K.; Froemming, G. R. A.; Hermawan, H. Cytotoxicity Evaluation of Biodegradable Zn-3Mg Alloy toward Normal Human Osteoblast Cells. *Mater. Sci. Eng. C* **2015**. https://doi.org/10.1016/j.msec.2015.01.056.

(12) Shearier, E. R.; Bowen, P. K.; He, W.; Drelich, A.; Drelich, J.; Goldman, J.; Zhao, F. In Vitro Cytotoxicity, Adhesion, and Proliferation of Human Vascular Cells Exposed to Zinc. *ACS Biomater. Sci. Eng.* **2016**, *2* (4), 634–642. https://doi.org/10.1021/acsbiomaterials.6b00035.

(13) Krones, C. J.; Klosterhalfen, B.; Butz, N.; Hoelzl, F.; Junge, K.; Stumpf, M.; Peiper, C.; Klinge, U.; Schumpelick, V. Effect of Zinc Pretreatment on Pulmonary Endothelial Cells in Vitro and Pulmonary Function in a Porcine Model of Endotoxemia. *J. Surg. Res.* **2005**, *123* (2), 251–256. https://doi.org/10.1016/J.JSS.2004.08.024.

(14) Ma, J.; Zhao, N.; Zhu, D. Bioabsorbable Zinc Ion Induced Biphasic Cellular Responses in Vascular Smooth Muscle Cells. *Sci. Rep.* **2016**, *6* (1), 26661. https://doi.org/10.1038/srep26661.

(15) Zhu, D.; Su, Y.; Young, M. L.; Ma, J.; Zheng, Y.; Tang, L. Biological Responses and Mechanisms of Human Bone Marrow Mesenchymal Stem Cells to Zn and Mg Biomaterials. *ACS Appl. Mater. Interfaces* **2017**, *9* (33), 27453–27461. https://doi.org/10.1021/acsami.7b06654.

(16) Bakhsheshi-Rad, H. R.; Hamzah, E.; Low, H. T.; Kasiri-Asgarani, M.; Farahany, S.; Akbari, E.; Cho, M. H. Fabrication of Biodegradable Zn-Al-Mg Alloy: Mechanical Properties, Corrosion Behavior, Cytotoxicity and Antibacterial Activities. *Mater. Sci. Eng. C* **2017**, *73*, 215–219. https://doi.org/10.1016/j.msec.2016.11.138.

(17) Zhao, C.; Wu, H.; Hou, P.; Ni, J.; Han, P.; Zhang, X. Enhanced Corrosion Resistance and Antibacterial Property of Zn Doped DCPD Coating on Biodegradable Mg. *Mater. Lett.* **2016**, *180*, 42–46. https://doi.org/10.1016/J.MATLET.2016.04.035.

(18) Yang, H.; Qu, X.; Lin, W.; Wang, C.; Zhu, D.; Dai, K.; Zheng, Y. In Vitro and in Vivo Studies on Zinc-Hydroxyapatite Composites as Novel Biodegradable Metal Matrix Composite for Orthopedic Applications. *Acta Biomater.* **2018**, *71*, 200–214. https://doi.org/10.1016/J.ACTBIO.2018.03.007.

(19) Surmenev, R. A.; Surmeneva, M. A.; Ivanova, A. A. Significance of Calcium Phosphate Coatings for the Enhancement of New Bone Osteogenesis – A Review. *Acta Biomater.* **2014**, *10* (2), 557–579. https://doi.org/10.1016/j.actbio.2013.10.036.

(20) Cozzolino, M.; Dusso, A. S.; Slatopolsky, E. Role of Calcium-Phosphate Product and Bone-Associated Proteins on Vascular Calcification in Renal Failure. *J. Am. Soc. Nephrol.* **2001**, *12* (11), 2511–2516.

(21) Liu, B.; Zhang, X.; Xiao, G. Y.; Lu, Y. P. Phosphate Chemical Conversion Coatings on Metallic Substrates for Biomedical Application: A Review. *Materials Science and Engineering C*. Elsevier Ltd February 1, 2015, pp 97–104. https://doi.org/10.1016/j.msec.2014.11.038.

(22) Su, Y.; Wang, K.; Gao, J.; Yang, Y.; Qin, Y. X.; Zheng, Y.; Zhu, D. Enhanced Cytocompatibility and Antibacterial Property of Zinc Phosphate Coating on Biodegradable Zinc Materials. *Acta Biomater.* **2019**. https://doi.org/10.1016/j.actbio.2019.03.055.

(23) Ross, J. M. Cell-Extracellular Matrix Interactions. In *Frontiers in Tissue Engineering*; Elsevier, 1998; pp 15–27. https://doi.org/10.1016/b978-008042689-1/50004-2.

(24) Oliver, J. anne N.; Su, Y.; Lu, X.; Kuo, P. H.; Du, J.; Zhu, D. Bioactive Glass Coatings on Metallic Implants for Biomedical Applications. *Bioactive Materials*. KeAi Communications Co. December 1, 2019, pp 261–270. https://doi.org/10.1016/j.bioactmat.2019.09.002.

(25) El-Fiqi, A.; Kim, T. H.; Kim, M.; Eltohamy, M.; Won, J. E.; Lee, E. J.; Kim, H. W. Capacity of Mesoporous Bioactive Glass Nanoparticles to Deliver Therapeutic Molecules. *Nanoscale* **2012**. https://doi.org/10.1039/c2nr31775c.

(26) Pajares-Chamorro, N.; Chatzistavrou, X. Bioactive Glass Nanoparticles for Tissue Regeneration. *ACS Omega* **2020**. https://doi.org/10.1021/acsomega.0c00180.

(27) Tian, M.; Chen, F.; Song, W.; Song, Y.; Chen, Y.; Wan, C.; Yu, X.; Zhang, X. In Vivo Study of Porous Strontium-Doped Calcium Polyphosphate Scaffolds for Bone Substitute Applications. *J. Mater. Sci. Mater. Med.* **2009**. https://doi.org/10.1007/s10856-009-3713-5.

(28) Stähli, C.; James-Bhasin, M.; Hoppe, A.; Boccaccini, A. R.; Nazhat, S. N. Effect of Ion Release from Cu-Doped 45S5 Bioglass® on 3D Endothelial Cell Morphogenesis. *Acta Biomater.* **2015**. https://doi.org/10.1016/j.actbio.2015.03.009.

(29) Pajares-Chamorro, N.; Wagley, Y.; Maduka, C. V.; Youngstrom, D. W.; Yeger, A.; Badylak, S. F.; Hammer, N. D.; Hankenson, K.; Chatzistavrou, X. Silver-Doped Bioactive Glass Particles for in Vivo Bone Tissue Regeneration and Enhanced Methicillin-Resistant Staphylococcus Aureus (MRSA) Inhibition. *Mater. Sci. Eng. C* **2020**. https://doi.org/10.1016/j.msec.2020.111693.

(30) Pajares-Chamorro, N.; Shook, J.; Hammer, N. D.; Chatzistavrou, X. Resurrection of Antibiotics That Methicillin-Resistant Staphylococcus Aureus Resists by Silver-Doped Bioactive Glass-Ceramic Microparticles. *Acta Biomater.* **2019**. https://doi.org/10.1016/j.actbio.2019.07.012.

(31) Hernández-Escobar, D.; Unocic, R. R.; Kawasaki, M.; Boehlert, C. J. High-Pressure Torsion Processing of Zn–3Mg Alloy and Its Hybrid Counterpart: A Comparative Study. *J. Alloys Compd.* **2020**, *831*, 154891. https://doi.org/10.1016/j.jallcom.2020.154891.

(32) Tyona, M. D. A Theoritical Study on Spin Coating Technique. *Adv. Mater. Res.* **2013**, *2* (4), 195–208. https://doi.org/10.12989/amr.2013.2.4.195.

(33) Pajares-Chamorro, N.; Hernández-Escobar, S.; Wagley, Y.; Acevedo, P.; Cramer, M.; Badylak, S.; Hammer, N. D.; Hardy, J.; Hankenson, K.; Chatzistavrou, X. Silver-Releasing Bioactive Glass Nanoparticles for Infected Tissue Regeneration. *Biomater. Adv.* **2023**, *154*, 213656. https://doi.org/10.1016/j.bioadv.2023.213656.

(34) Sakata, O.; Nakamura, M. Grazing Incidence X-Ray Diffraction. In *Springer Series in Surface Sciences*; 2013; pp 165–190. https://doi.org/10.1007/978-3-642-34243-1_6.

(35) ASTM G31-12a - Standard Guide for Laboratory Immersion Corrosion Testing of Metals.

https://doi.org/10.1520/G0031-12A.

(36) ASTM. ASTM G1-03: Standard Practice for Preparing, Cleaning, and Evaluating Corrosion Test Specimens. *ASTM Spec. Tech. Publ.* **2017**, *i*, 505–510. https://doi.org/10.1520/G0001-03R17E01.2.

(37) ISO 10993-5: Biological Evaluation of Medical Devices - Tests for in Vitro Cytotoxicity. *ISO Stand.* **2009**.

(38) Wang, J.; Witte, F.; Xi, T.; Zheng, Y.; Yang, K.; Yang, Y.; Zhao, D.; Meng, J.; Li, Y.; Li, W.; et al. Recommendation for Modifying Current Cytotoxicity Testing Standards for Biodegradable Magnesium-Based Materials. *Acta Biomater.* **2015**, *21*, 237–249. https://doi.org/10.1016/j.actbio.2015.04.011.

(39) Fey, P. D.; Endres, J. L.; Yajjala, V. K.; Widhelm, T. J.; Boissy, R. J.; Bose, J. L.; Bayles, K. W. A Genetic Resource for Rapid and Comprehensive Phenotype Screening of Nonessential Staphylococcus Aureus Genes. *MBio* **2013**. https://doi.org/10.1128/mBio.00537-12.

(40) Flegler, S. L.; Heckman, J. W.; Klomparens, K. L. *Scanning and Transmission Electron Microscopy: An Introduction*; Oxford University Press, 1994. https://doi.org/10.5860/CHOICE.31-4353.

(41) Bowen, P. K.; Drelich, J.; Goldman, J. Zinc Exhibits Ideal Physiological Corrosion Behavior for Bioabsorbable Stents. *Adv. Mater.* **2013**. https://doi.org/10.1002/adma.201300226.

(42) Li, G. Y.; Lian, J. S.; Niu, L. Y.; Jiang, Z. H.; Jiang, Q. Growth of Zinc Phosphate Coatings on AZ91D Magnesium Alloy. *Surf. Coatings Technol.* **2006**, *201* (3–4), 1814–1820. https://doi.org/10.1016/j.surfcoat.2006.03.006.

(43) Geißler, U.; Hempel, U.; Wolf, C.; Scharnweber, D.; Worch, H.; Wenzel, K. W. Collagen Type I-Coating of Ti6A14V Promotes Adhesion of Osteoblasts. *J. Biomed. Mater. Res.* **2000**, *51* (4), 752–760. https://doi.org/10.1002/1097-4636(20000915)51:4<752::AID-JBM25>3.0.CO;2-7.

(44) Zhao, N.; Zhu, D. Collagen Self-Assembly on Orthopedic Magnesium Biomaterials Surface and Subsequent Bone Cell Attachment. *PLoS One* **2014**, *9* (10), e110420. https://doi.org/10.1371/journal.pone.0110420.

(45) Brodie, J. C.; Goldie, E.; Connel, G.; Merry, J.; Grant, M. H. Osteoblast Interactions with Calcium Phosphate Ceramics Modified by Coating with Type I Collagen. *J. Biomed. Mater. Res. - Part A* **2005**. https://doi.org/10.1002/jbm.a.30279.

(46) Guo, Y.; Su, Y.; Gu, R.; Zhang, Z.; Li, G.; Lian, J.; Ren, L. Enhanced Corrosion Resistance and Biocompatibility of Biodegradable Magnesium Alloy Modified by Calcium Phosphate/Collagen Coating. *Surf. Coatings Technol.* **2020**. https://doi.org/10.1016/j.surfcoat.2020.126318.

(47) Xia, W.; Chang, J. Preparation and Characterization of Nano-Bioactive-Glasses (NBG) by a Quick Alkali-Mediated Sol-Gel Method. *Mater. Lett.* **2007**. https://doi.org/10.1016/j.matlet.2006.11.048.

(48) Luz, G. M.; Mano, J. F. Nanoengineering of Bioactive Glasses: Hollow and Dense Nanospheres. *J. Nanoparticle Res.* **2013**. https://doi.org/10.1007/s11051-013-1457-0.

(49) Liu, L.; Meng, Y.; Dong, C.; Yan, Y.; Volinsky, A. A.; Wang, L.-N. Initial Formation of Corrosion Products on Pure Zinc in Simulated Body Fluid. *J. Mater. Sci. Technol.* **2018**. https://doi.org/10.1016/J.JMST.2018.05.005.

(50) Li, P.; Dai, J.; Schweizer, E.; Rupp, F.; Heiss, A.; Richter, A.; Klotz, U. E.; Geis-Gerstorfer, J.; Scheideler, L.; Alexander, D. Response of Human Periosteal Cells to Degradation Products of Zinc and Its Alloy. *Mater. Sci. Eng. C* **2020**, *108*. https://doi.org/10.1016/j.msec.2019.110208.

(51) Su, Y.; Yang, H.; Gao, J.; Qin, Y.; Zheng, Y.; Zhu, D. Interfacial Zinc Phosphate Is the Key to Controlling Biocompatibility of Metallic Zinc Implants. *Adv. Sci.* **2019**, 1900112. https://doi.org/10.1002/advs.201900112.

(52) Dargusch, M. S.; Venezuela, J.; Dehghan-Manshadi, A.; Johnston, S.; Yang, N.; Mardon, K.; Lau, C.; Allavena, R. In Vivo Evaluation of Bioabsorbable Fe-35Mn-1Ag: First Reports on In Vivo Hydrogen Gas Evolution in Fe-Based Implants. *Adv. Healthc. Mater.* **2021**, *10* (2). https://doi.org/10.1002/adhm.202000667.

(53) Elkaiam, L.; Hakimi, O.; Yosafovich-Doitch, G.; Ovadia, S.; Aghion, E. In Vivo Evaluation of Mg–5%Zn–2%Nd Alloy as an Innovative Biodegradable Implant Material. *Ann. Biomed. Eng.* **2020**, *48* (1), 380–392. https://doi.org/10.1007/s10439-019-02355-5.

(54) Zberg, B.; Uggowitzer, P. J.; Löffler, J. F. MgZnCa Glasses without Clinically Observable Hydrogen Evolution for Biodegradable Implants. *Nat. Mater.* **2009**, *8* (11), 887–891. https://doi.org/10.1038/nmat2542.

(55) Kim, Y.-K.; Lee, K.-B.; Kim, S.-Y.; Bode, K.; Jang, Y.-S.; Kwon, T.-Y.; Jeon, M. H.; Lee, M.-H. Gas Formation and Biological Effects of Biodegradable Magnesium in a Preclinical and Clinical Observation. *Sci. Technol. Adv. Mater.* **2018**, *19* (1), 324–335. https://doi.org/10.1080/14686996.2018.1451717.

(56) Li, P.; Schille, C.; Schweizer, E.; Rupp, F.; Heiss, A.; Legner, C.; Klotz, U. E.; Gerstorfer, J. G.; Scheideler, L. Mechanical Characteristics, in Vitro Degradation, Cytotoxicity, and Antibacterial Evaluation of Zn-4.0Ag Alloy as a Biodegradable Material. *Int. J. Mol. Sci.* **2018**. https://doi.org/10.3390/ijms19030755.

(57) Becker, D.; Geissler, U.; Hempel, U.; Bierbaum, S.; Scharnweber, D.; Worch, H.; Wenzel, K.-W. Proliferation and Differentiation of Rat Calvarial Osteoblasts on Type I Collagen-Coated Titanium Alloy. *J. Biomed. Mater. Res.* **2002**.

(58) Andrianarivo, A. G.; Robinson, J. A.; Mann, K. G.; Tracy, R. P. Growth on Type I Collagen Promotes Expression of the Osteoblastic Phenotype in Human Osteosarcoma MG-63 Cells. *J. Cell. Physiol.* **1992**. https://doi.org/10.1002/jcp.1041530205.

(59) Masi, L.; Franchi, A.; Santucci, M.; Danielli, D.; Arganini, L.; Giannone, V.; Formigli, L.; Benvenuti, S.; Tanini, A.; Beghe, F.; et al. Adhesion, Growth, and Matrix Production by Osteoblasts on Collagen Substrata. *Calcif. Tissue Int.* **1992**. https://doi.org/10.1007/BF00334548.

(60) Lorenzetti, M.; Dogša, I.; Stošicki, T.; Stopar, D.; Kalin, M.; Kobe, S.; Novak, S. The Influence of Surface Modification on Bacterial Adhesion to Titanium-Based Substrates. *ACS Appl. Mater. Interfaces* **2015**. https://doi.org/10.1021/am507148n.

(61) Wu, S.; Zhang, B.; Liu, Y.; Suo, X.; Li, H. Influence of Surface Topography on Bacterial Adhesion: A Review (Review). *Biointerphases* **2018**. https://doi.org/10.1116/1.5054057.

(62) Teughels, W.; Van Assche, N.; Sliepen, I.; Quirynen, M. Effect of Material Characteristics and/or Surface Topography on Biofilm Development. *Clin. Oral Implants Res.* **2006**. https://doi.org/10.1111/j.1600-0501.2006.01353.x.

(63) Song, Z.; Borgwardt, L.; Høiby, N.; Wu, H.; Sørensen, T. S.; Borgwardt, A. Prosthesis Infections after Orthopedic Joint Replacement: The Possible Role of Bacterial Biofilms. *Orthop. Rev. (Pavia).* **2013**, *5* (2), 14. https://doi.org/10.4081/or.2013.e14.

(64) He, T.; Shi, Z. L.; Fang, N.; Neoh, K. G.; Kang, E. T.; Chan, V. The Effect of Adhesive Ligands on Bacterial and Fibroblast Adhesions to Surfaces. *Biomaterials* **2009**. https://doi.org/10.1016/j.biomaterials.2008.09.049.

(65) Chatzistavrou, X.; Fenno, J. C.; Faulk, D.; Badylak, S.; Kasuga, T.; Boccaccini, A. R.; Papagerakis, P. Fabrication and Characterization of Bioactive and Antibacterial Composites for Dental Applications. *Acta Biomater.* **2014**. https://doi.org/10.1016/j.actbio.2014.04.030.

(66) Pajares-Chamorro, N.; Lensmire, J. M.; Hammer, N. D.; Hardy, J. W.; Chatzistavrou, X. Unraveling the Mechanisms of Inhibition of Silver-doped Bioactive Glass–Ceramic Particles. *J. Biomed. Mater. Res. Part A* **2023**, *111* (7), 975–994. https://doi.org/10.1002/jbm.a.37482.

(67) Feng, Q. L.; Wu, J.; Chen, G. Q.; Cui, F. Z.; Kim, T. N.; Kim, J. O. A Mechanistic Study of the Antibacterial Effect of Silver Ions on Escherichia Coli and Staphylococcus Aureus. *J. Biomed. Mater. Res.* **2000**. https://doi.org/10.1002/1097-4636(20001215)52:4<662::AID-JBM10>3.0.CO;2-3.

(68) Otto, C. C.; Cunningham, T. M.; Hansen, M. R.; Haydel, S. E. Effects of Antibacterial Mineral Leachates on the Cellular Ultrastructure, Morphology, and Membrane Integrity of Escherichia Coli and Methicillin-Resistant Staphylococcus Aureus. *Ann. Clin. Microbiol. Antimicrob.* **2010**. https://doi.org/10.1186/1476-0711-9-26.

TOC Graphic

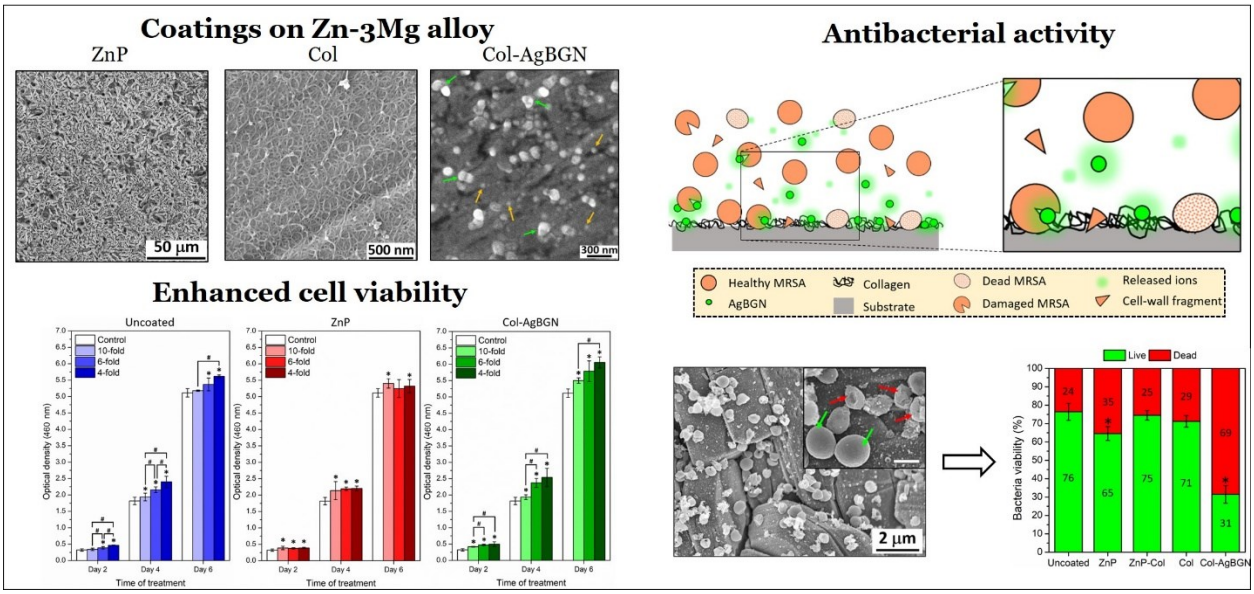
Coatings on Zn-3Mg alloy
ZnP
Col
Col-AgBGN
50 µm
500 nm
300 nm
Enhanced cell viability
Uncoated
ZnP
Col-AgBGN
Control
10-fold
6-fold
4-fold
Optical density (460 nm)
Day 2
Day 4
Day 6
Time of treatment
Antibacterial activity
Healthy MRSA
AgBGN
Collagen
Substrate
Dead MRSA
Damaged MRSA
Released ions
Cell-wall fragment
2 µm
Live
Dead
Bacteria viability (%)
24
76
35
65
25
75
29
71
69
31
Uncoated
ZnP
ZnP-Col
Col
Col-AgBGN